Simulations of Subtropical Cyclones in a Baroclinic Channel Model

CHRISTOPHER A. DAVIS

National Center for Atmospheric Research, Boulder, Colorado*

(Manuscript received 14 December 2009, in final form 4 May 2010)

ABSTRACT

The present study considers a variety of cyclone developments that occur in an idealized, baroclinic channel model featuring full condensation heating effects over an ocean with prescribed sea surface temperature variation. The geostrophic basic-state jet is specified by the tropopause shape, and horizontal shear is included by specifying the meridional variation of zonal wind on the lower boundary. The horizontal shear induces anticyclonic wave breaking of baroclinic waves. Normal mode perturbations are computed using a ''fake-dry'' version of the model but integrated forward using full physics.

Low-latitude moist convection is particularly strong in simulations with strong surface easterlies that destabilize the troposphere through water vapor fluxes from the ocean surface. Deep convection produces a locally elevated dynamic tropopause and an associated anticyclone. This modified zonal flow supports moist baroclinic instability. The resulting cyclones, identified as subtropical cyclones, occur in deep westerly vertical wind shear but are nearly devoid of lower-tropospheric baroclinicity initially. These systems are distinguished from baroclinically dominated secondary cyclones that also form at relatively low latitudes in the simulations.

For weak jets and strong subtropical surface easterlies, subtropical cyclone development dominates formation on the midlatitude jet. For strong westerly jets or weak horizontal shear, the situation is reversed and the midlatitude baroclinic wave can help or hinder the ultimate intensification of the subtropical cyclone. The similarity of this cross-latitude influence to the extratropical transition of tropical cyclones is noted.

1. Introduction

What are subtropical cyclones? Cyclones forming in the subtropics, roughly 23–35° from the equator, have long presented challenges for basic understanding, classification, and forecasting. They have been regarded as having some characteristics of extratropical and tropical cyclones simultaneously. As noted by Evans and Guishard (2009) and Guishard et al. (2009), they are inconsistently included in the database for tropical cyclones. Their distinction from conventional extratropical cyclones is subtle. Cyclone phase space (CPS) diagrams (Hart 2003) suggest that these disturbances develop in baroclinic environments but that the baroclinicity is relatively shallow and weak compared to that in cool season midlatitude cyclones. Furthermore, deep moist convection is thought to influence subtropical cyclones fundamentally, yet this contribution has not been quantified.

To set the context for a study of subtropical cyclones, the dependence of the life cycle of cyclones on condensation heating, baroclinicity, and meridional shear of the zonal wind is first reviewed. Idealized baroclinic wave simulations have revealed the existence of a variety of cyclone types even without the condensation process. Davies et al. (1991), Thorncroft et al. (1993), and Wernli et al. (1998) identified distinct paradigms of cyclone development depending on the sign and strength of the barotropic shear added to a midlatitude jet. The Rossby waves exhibited wave breaking that mirrored the sense of the shear. Cyclonic wave breaking in cyclonic barotropic shear resulted in large, deep cyclones. Anticyclonic wave breaking in anticyclonic shear resulted in strong anticyclones and anticyclonically curved filaments of potential vorticity (PV) in the upper troposphere. This picture has been clarified and modified somewhat in more recent work by Orlanski (2003), who emphasized the importance of surface baroclinicity and the intensity

* The National Center for Atmospheric Research is sponsored by the National Science Foundation.

Corresponding author address: Christopher A. Davis, P.O. Box 3000, Boulder, CO 80307.
E-mail: cdavis@ucar.edu

DOI: 10.1175/2010JAS3411.1

of surface cyclone development in determining whether waves break cyclonically or anticyclonically. Still, the basic paradigm of wave-breaking dichotomy has enjoyed considerable utility.

A curious result of simulations in anticyclonic shear is the appearance of secondary cyclone formation where the end of the upper-tropospheric PV filament, having amalgamated into a closed low, approaches a surface baroclinic zone (Simmons and Hoskins 1978; Thorncroft and Hoskins 1990). This secondary cyclone occurs far to the south of the primary cyclone growing on the midlatitude jet. The real-world counterpart of this type of cyclone is probably the kona low (Daingerfield 1921; Simpson 1952; Otkin and Martin 2004) and cyclones with similar evolution that occur at other longitudes. Occasionally these cyclones become tropical cyclones (Davis and Bosart 2003). The basic dynamics of these cyclones, at least initially, is still baroclinic. Cyclones like these are often termed subtropical cyclones because of the latitude range in which they occur.

The addition of moisture introduces considerable complexity to the cyclone problem even in the context of idealized simulations. It is well known that condensation heating can destabilize short length scales with respect to adiabatic baroclinic instability (Whitaker and Davis 1994). In fact, the growth rate of disturbances becomes relatively independent of wavelength with condensation heating (exactly so in the two-dimensional case). Condensation decreases the horizontal length scale of ordinary baroclinic waves (Emanuel et al. 1987). It also gives rise to entirely new phenomena such as diabatic Rossby waves (Parker and Thorpe 1995; Wernli et al. 2002) and diabatic Rossby vortices (DRVs; Moore and Montgomery 2005). The latter form in the presence of strong condensation heating and modest vertical wind shear. A close cousin of the DRV is the mesoscale convective vortex (MCV) that forms from organized mesoscale convection, and through baroclinic processes may engender and organize new convection (Raymond and Jiang 1990). As may be inferred from Conzemius et al. (2007), there is a duality between coherent vortices emerging from organized convection and the development of cyclones with relatively short length scales. This duality is partly due to the short-wave destabilization produced by condensation heating. Short-wavelength cyclones with strong condensation heating contain closed PV contours at finite amplitude due to condensation heating. These systems exhibit both wavelike and vortexlike characteristics. The distinction between convective systems and baroclinic cyclones becomes blurred. Untangling this duality is central to understanding the dynamical identity of phenomena such as subtropical cyclones in which condensation processes are prominent.

The present paper attempts to clarify the dynamical characteristics of subtropical cyclones through the use of an idealized baroclinic channel model with parameterized effects of condensation heating. The model is the Advanced Research Weather Research and Forecasting model (ARW-WRF, hereafter ARW), configured as described in section 2. A baroclinic jet whose strength is systematically varied is introduced. Horizontal shear, of varying strengths in different simulations, is introduced in an attempt to induce anticyclonic wave breaking. Abundant moisture is present because the entire domain is over ocean whose surface temperature is controlled by the initial north–south temperature variation. The aim of the study is to see what cyclone structures develop equatorward of the primary cyclone that forms within the midlatitude jet and to understand the basic mechanism of formation of these cyclones.

The paper defines a set of diagnostic methods that help to explain how the origin of subtropical cyclones departs from the formation of midlatitude cyclones (section 2). The basic effect of condensation in contrasting pairs of simulations is evaluated in section 3. Section 4 elucidates the development paths of several cyclones and quantifies the formation of one subtropical cyclone in particular. Section 5 rounds out the parameter space of varying meridional shear, midlatitude jet strength, and condensation heating. The dichotomous behavior of these simulations regarding whether extratropical or subtropical systems dominate the long-term solution is summarized in section 6.

2. Methods

The ARW is a nonhydrostatic, primitive equation model described in Skamarock et al. (2005). The present application is in an idealized framework that is similar to the generic baroclinic wave test case available in WRF. However, the present model configurations are relatively more complex.

The model atmosphere is divided into a troposphere and stratosphere following Plougonven and Snyder (2007), who built on work by Rotunno et al. (1994) and Heckley and Hoskins (1982). The PV distribution in the initially purely zonal flow is specified by the height of the tropopause, which is a hyperbolic tangent profile in the y direction, centered at the latitude of the westerly jet y_J. The PV in the troposphere is not uniform because of the addition of $\beta = df/dy$, where f is the Coriolis parameter. Here, β is fixed at 10^{-11} m^{-1} s^{-1}. The PV is inverted for the wind and potential temperature fields, which are assumed to be in geostrophic balance. The boundary conditions on the zonal velocity are homogeneous except for the lower boundary upon which a meridionally

varying zonal mean wind is prescribed. This constitutes the inclusion of ''barotropic'' shear in the model, although the meridional shear in the final state will not be strictly barotropic. Thus, we refer to this as horizontal shear or ''bottom shear,'' although the shear will have units of velocity and represent the amplitude of the sinusoidally varying zonal surface wind. The surface zonal wind is specified poleward of y_0 as $\overline{u}_S = -S\sin[2\pi(y - y_0)/(D - y_0)]$, where D is the full meridional extent of the model domain (10 000 km) and S is the amplitude of the shear. The upper-tropospheric jet is centered at $(D + y_0)/2$ such that the anticyclonic shear is maximized at the location of the jet. The initial surface wind is set to zero south of y_0, where $y_0 = 1000$ km. Examples of the initial basic-state zonal flow appear in Fig. 1. The parameters varied are the amplitude of the tropopause transition, which translates nearly linearly into a maximum jet speed U, and S. The nomenclature for simulations is Smm_Unn, where mm refers to the value of S and nn is the strength of the initial U (Table 1). Hence, S15_U30 is a simulation with a bottom shear of amplitude 15 m s^{-1} and 30 m s^{-1} westerly jet at the tropopause.[1] We also use a suffix D to denote a ''fake-dry'' integration. In these fake-dry simulations, surface heat, moisture, and momentum fluxes remain on, but there is no condensation heating or cooling. In some simulations, condensation heating is removed after a specific time. These simulations are referred to by appending this time in hours after D.

The model domain is periodic in the x direction with a domain length of 4000 km. The horizontal grid spacing for the simulations presented is 50 km. There are 60 vertical levels, stretched between a vertical spacing of about 100 m near the surface to greater than 500 m at the model top at 27 km. The model is initialized with a fake-dry, adiabatic, nearly inviscid normal mode obtained by a breeding method (Plougonven and Snyder 2007). Surface fluxes are turned off during the integration of the normal mode. The initial maximum amplitude of the mode, which occurs at the tropopause, is set to 2 K. Some simulations will be integrated with infinitesimal initial amplitude as described in section 4.

The model is integrated forward with physical parameterizations that include the Kain–Fritsch cumulus parameterization (Kain 2004), the Yonsei University boundary layer scheme (Noh et al. 2003), and the WRF single-moment microphysics scheme (WSM5), which predicts rain, snow, cloud water, and cloud ice but only distinguishes liquid and ice phases based on temperature. Horizontal mixing is treated with a two-dimensional deformation-dependent mixing coefficient as well as a sixth-order hyperdiffusion with a constant coefficient.

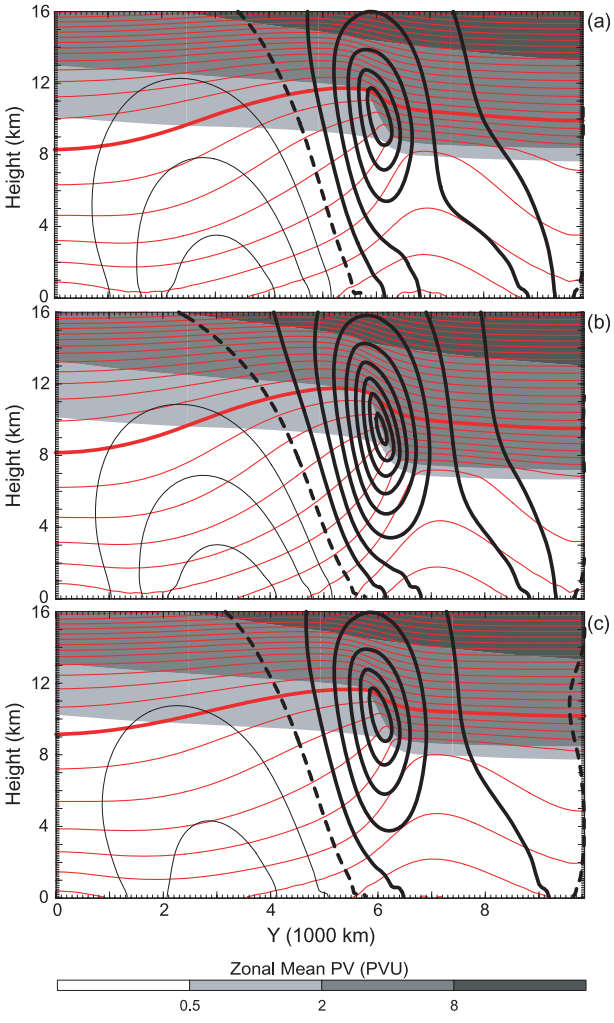

FIG. 1. Zonally averaged zonal wind [black contours; contour interval (CI) = 5 m s^{-1}), θ (red, CI = 5 K) and PV (grayscale; PVU) for (a) S15_U30, (b) S15_U40, and (c) S10_U30 at $t = 0$ h. Thick red line is 330-K isentrope; thick dashed line is zero wind line. Flow into the page is shown with thin solid lines.

The model domain is entirely over ocean, with the sea surface temperature (SST) prescribed to be 0.5 K greater than the initial atmospheric temperature at the lowest model level (about 40 m MSL). The SST will therefore vary among the different experiments according to the baroclinicity. To maintain some consistency between simulations we adjust the basic state so that the maximum SST in the domain is close to 30°C. The tropospheric humidity is uniformly 50% so that the maximum water vapor mixing ratio in each simulation is initially about the same. In the warmer regions, the initial moist thermodynamic

[1] After interpolations and an initialization procedure to remove spurious oscillations (Plougonven and Snyder 2007), the actual jet maximum speed may deviate by up to 1 m s^{-1} from the number indicated in the name of the simulation.

TABLE 1. Simulations analyzed in the present study. Units for U and S are meters per second. Simulation names appear in the appropriate cells. A dash indicates that no simulation was performed for that combination of parameters. Suffix D120 refers to simulation that is run in fake-dry configuration after 120 h; suffix C refers to simulations with temperature reduced by 5 K; suffix NOMODE refers to simulation with initial mode amplitude set to 0.001 K; suffix GD refers to the use of the Grell–Devenyi cumulus scheme; and suffix DX25 refers to simulation S15_U40_NOMODE run with a grid spacing of 25 km.

	$U = 25$	$U = 30$	$U = 35$	$U = 40$	$U = 50$
$S = 5$	—	S05_U30	—	—	—
$S = 10$	—	S10_U30	—	S10_U40	—
$S = 15$	S15_U25	S15_U30, S15_U30_D, S15_U30_D120, S15_U30_C	S15_U35	S15_U40, S15_U40_D, S15_U40_D120, S15_U40_NOMODE, S15_U40_C, S15_U40_GD, S15_U40_DX25	S15_U50

stability is nearly the same in all simulations as a result. Substantial conditional instability, represented by convective available potential energy (CAPE), exists in the initial state over the warmest water in the domain and is generally released before the mode on the jet grows to appreciable amplitude. Significant convective inhibition (CIN) also exists at the start of each simulation but it is reduced because of fluxes from the ocean surface. The strength of the initial surface winds is directly proportional to S. Deep convection breaks out sooner for stronger bottom shear and does so in easterly flow.

A variety of cyclones develop in the various simulations performed and these are analyzed in a cyclone-following framework. We first utilize a cyclone tracking algorithm (Davis et al. 2008). Vorticity at 900 hPa at all points is first replaced by the average over an 11×11 gridpoint box (500 km $\times$ 500 km) centered on each point. Maxima in area-averaged vorticity are tracked using a 6-h time interval, and parameters are computed in a system-following frame of reference. Vorticity maxima must attain values of 2×10^{-5} s^{-1} to be included.

The tracking algorithm uses the linear extrapolation of cyclone motion over the previous 12 h as a guess for the position 6 h hence. If a vorticity maximum exceeding the intensity constraint is found within 400 km of this position, it is assigned as a continuation of the previous vorticity maximum. If no vorticity maximum is found, the track ends. If a vorticity maximum is found with no preceding position, it is tracked as a new feature.

Because condensation heating is significant for the oceanic cyclones in the simulations, it is useful to know how the relative importance of condensation heating and baroclinic processes changes from storm to storm, and during the life cycle of a given cyclone. Two existing measures of these contributions avail themselves. First is the energy conversion diagnostic (Lorenz 1955; Parker and Thorpe 1995; Moore and Montgomery 2005) wherein the rates of generation of eddy available potential energy (APE) by diabatic processes and conversion of mean available potential energy are compared. Another commonly used diagnostic is the phase space diagram (Hart 2003), in which the instantaneous structure of the cyclone is described using parameters that measure the lower-tropospheric geostrophic vertical wind shear and the vertical structure of the layer thickness anomalies above the cyclone center.

The energy conversion diagnostic provides time tendency information and quantifies the diabatic heating contribution to the generation of eddy APE through the correlation of heating and temperature anomalies. The adiabatic contribution is proportional to the meridional heat flux, tempered by the adiabatic cooling term that generally opposes this flux. In essence, this term measures the instantaneous meridional movement of isentropes by eddies. In contrast, the cyclone phase space diagram describes the structure of the cyclone itself but only indirectly indicates the processes involved.

In the present study we utilize a different metric that is based on Ertel PV, generalized to include potential temperature anomalies on the lower boundary, in practice at the top of the planetary boundary layer (around 900 hPa). Bretherton (1966) was the first to recognize formally that an inhomogeneous surface potential temperature distribution was equivalent to a homogeneous distribution plus a sheet of infinite PV an infinitesimal distance above the ground. This uses the fact that a discontinuous jump in potential temperature is synonymous with a delta function in PV. The resulting PV has a finite vertical integral and thus may be compared to a vertically integrated PV anomaly that exists elsewhere in the flow. The advantage of casting lower-boundary temperature anomalies in terms of PV is that baroclinic and condensation heating influences on cyclone structure can be compared directly. The near-surface baroclinicity is represented as a PV anomaly defined as follows:

$$\mathrm{PV1} = g\eta G/\Delta p_{\mathrm{ref}}, \tag{1}$$

where

$$G = (G_x^2 + G_y^2)^{1/2},$$

$$G_x = \frac{1}{L}\int_{-L/2}^{L/2} \theta'\, dy\bigg|_{x=L/2} - \frac{1}{L}\int_{-L/2}^{L/2} \theta'\, dy\bigg|_{x=-L/2},$$

$$G_y = \frac{1}{L}\int_{-L/2}^{L/2} \theta'\, dx\bigg|_{y=L/2} - \frac{1}{L}\int_{-L/2}^{L/2} \theta'\, dx\bigg|_{y=-L/2},$$

η is the absolute vorticity, and θ' is the deviation of potential temperature from the zonal mean. The coordinate (0, 0) is the cyclone center. The potential temperature variations (G_x, G_y) are averaged at two pressure levels, 900 and 850 hPa, prior to computing G. Furthermore, L = 1000 km and the vertical scale Δp_{ref} is chosen to be 400 hPa to match the range of vertical integration of interior PV (see below).

The interior PV, representing primarily the condensation heating influence, is defined by the volume integral of perturbation PV:

$$\text{PV2} = \frac{\int_{-L/2}^{L/2} dx \int_{-L/2}^{L/2} dy \int_{p_1}^{p_2} q'\, dp}{L^2 \Delta p_{\text{ref}}}, \qquad (2)$$

where q' is the deviation of PV from the zonal mean, p_1 = 500 hPa and p_2 = 900 hPa, and $\Delta p_{\text{ref}} = p_2 - p_1$. Averaging between these pressure levels generally avoids contributions to the PV from tropopause undulations. In general, we examine the ratio PV1/PV2, in which Δp_{ref} does not appear explicitly.

The goal in devising the PV metric is to have a simple measure of the contributions of lower-tropospheric baroclinic processes and condensation heating to the behavior of cyclones. Although the parameters are evaluated instantaneously, they embody the accumulated effects of baroclinic and condensation processes. Furthermore, time dependence of these parameters gives insight into the changing character of individual cyclones. This is qualitatively similar to some of the information obtained from cyclone phase space diagrams. It should be noted that these PV metrics cannot generally provide dynamical information about cause and effect. For instance, it is entirely possible that weak baroclinicity can still catalyze intense condensation heating.

To understand how the baroclinic dynamics are linked to thermodynamic destabilization and the organization of deep convection, we use the quasigeostrophic omega equation (Bluestein 1992):

$$\sigma \nabla^2 \omega + f_0^2 \frac{\partial^2 \omega}{\partial p^2} = -2\mathbf{V} \cdot \mathbf{Q}, \qquad (3)$$

where $\sigma[=(\kappa\pi/p)(\partial\Theta/\partial p)]$ is the quasigeostrophic stability parameter, $\kappa = R/C_p$, π is the Exner function, $\mathbf{Q}\{=-(R/p)[(\partial \mathbf{v}_g/\partial x) \cdot \nabla_p T,\ (\partial \mathbf{v}_g/\partial y) \cdot \nabla_p T]\}$ is the $\mathbf{Q}$ vector computed on pressure surfaces, subscript g denotes geostrophic, and the constant f_0 is the average value of the Coriolis parameter in the domain ($=10^{-4}$ s^{-1}). The variation of the Coriolis parameter has also been neglected on the right-hand side of (3). The stability parameter at each level represents the horizontal average across the domain. Periodic boundary conditions in the zonal direction and homogeneous upper and lower boundary conditions on ω are applied, with the top at 100 hPa. A relaxation solver is used, obtained from the Read/Interpolate/Plot program of the WRF system.

3. Large-scale effects of condensation

In Fig. 2, snapshots during the evolution of four different simulations are presented. The simulations with a weaker jet, S15_U30 and S15_U30_D (Figs. 2a,c), produce notably different solutions both from each other and from the solutions with the 40 m s^{-1} jet (Figs. 2b,d). The solution in S15_U30_D somewhat resembles the solution in S15_U40_D but grows more slowly and hence is less amplified at a given time. The surface fronts are comparatively weak and do not penetrate into lower latitudes at this point.

Simulation S15_U30 produces a strong cyclone (C_1) that forms in the easterlies around y = 3000 km and rapidly intensifies and turns northward (Fig. 2a). The evolution of C_1 is shown in Fig. 3. This cyclone begins at lower latitudes as an inverted trough in easterly flow by day 5 (Fig. 3a). It rapidly intensifies with strong diabatic heating and minimal near-surface baroclinicity (not shown) to become a deep cyclone by day 8 (Figs. 3b,c). The strong diabatic heating produces a deep column of cyclonic PV as indicated by PV greater than 2 PV units (PVU; 1 PVU = 10^{-6} m^2 K^{-1} kg^{-1} s^{-1}) even visible on the 330-K surface (8–9-km altitude) within the cyclone circulation starting at day 6.5. Cyclonic PV extending to this altitude has been observed in hurricanes (Shapiro and Franklin 1995). The development of C_1 appears independent of development on the midlatitude jet.

Cyclone C_1 also dominates the PV changes in the upper troposphere where the appearance of anticyclonically curved outflow (not shown) provides a strong upper-tropospheric ridge while at the same time contributing to the southward extrusion of a narrowing PV filament (Fig. 2a). This filament is associated with a weak surface disturbance and area of convection in easterly flow. The cyclone that grows from this disturbance (C_2) will be discussed below. Of note is that, despite the anticyclonic shear, the effect of condensation heating has resulted in a dominance of cyclonic circulation in the lower troposphere, as well as even stronger anticyclonic PV signatures

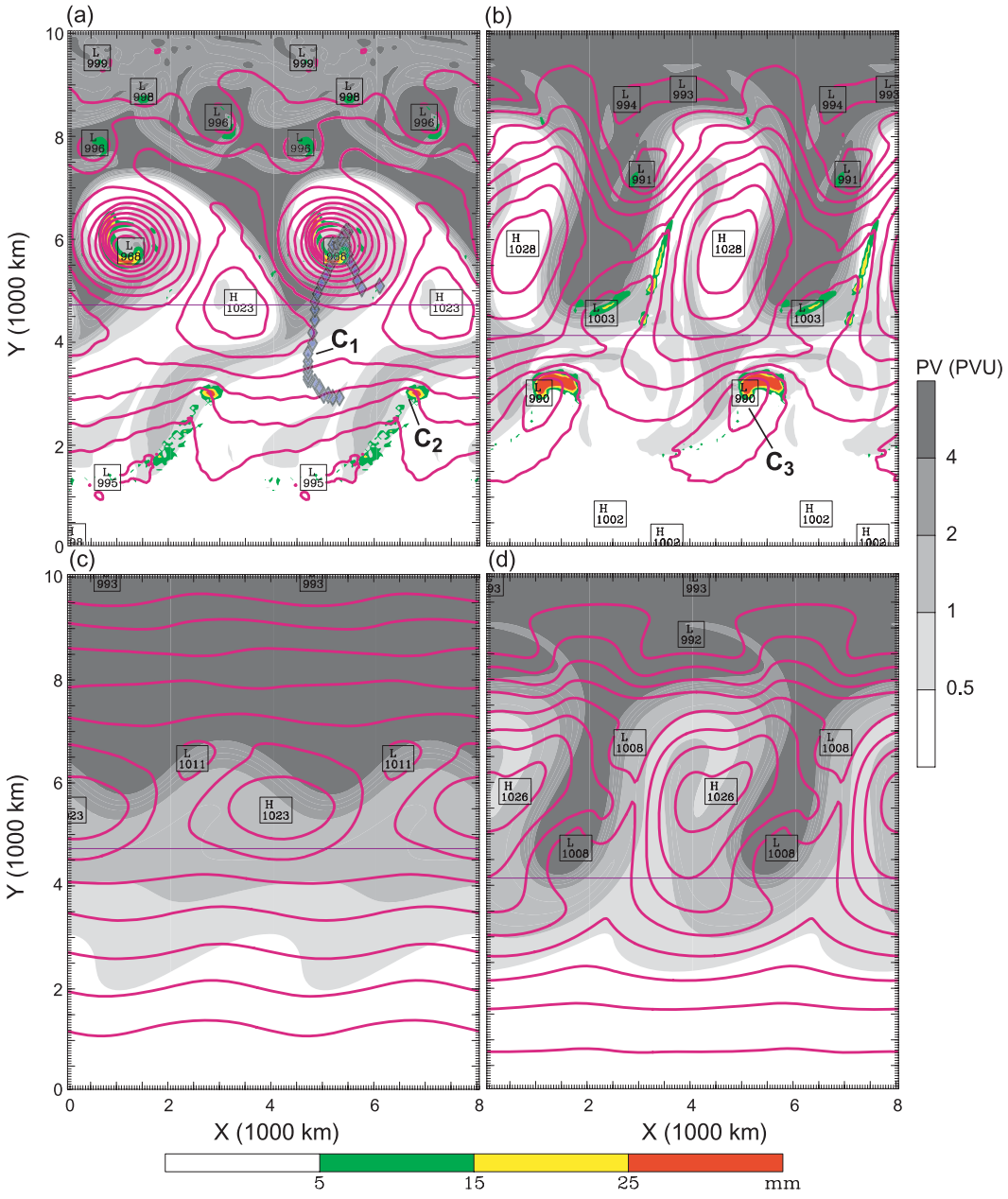

FIG. 2. PV on 330-K isentropic surface (grayscale; PVU), 6-h precipitation (color; mm) and SLP (magenta; CI = 4 hPa) for (a) S15_U30 at 240 h, (b) S15_U40 at 264 h, (c) S15_U30_D at 240 h, and (d) S15_U40_D at 264 h. Domain has been repeated in the x direction to more clearly show structures. Thin purple zonal line between y = 4000 km and y = 5000 km denotes the 26°C SST isotherm. The string of blue diamonds in (a) is the track of C_1 with positions shown every 6 h.

in the upper troposphere than are produced in the fake-dry simulation. This is consistent with the expected rearrangement of PV from condensation heating, wherein the PV in the upper troposphere decreases and PV in the lower troposphere increases.

Simulations S15_U40 and S15_U40_D (bottom shear amplitude 15 m s^{-1}, westerly jet 40 m s^{-1}, "D" for fake-dry; see section 2) are generally similar to each other at 264 h (Figs. 2b,d). The bottom shear has induced anticyclonic wave breaking seen in the PV and led to the dominance of the anticyclones over cyclones. The primary baroclinic cyclone that represents the evolution of the normal mode has progressed well into the nonlinear regime and has migrated to the far northern part

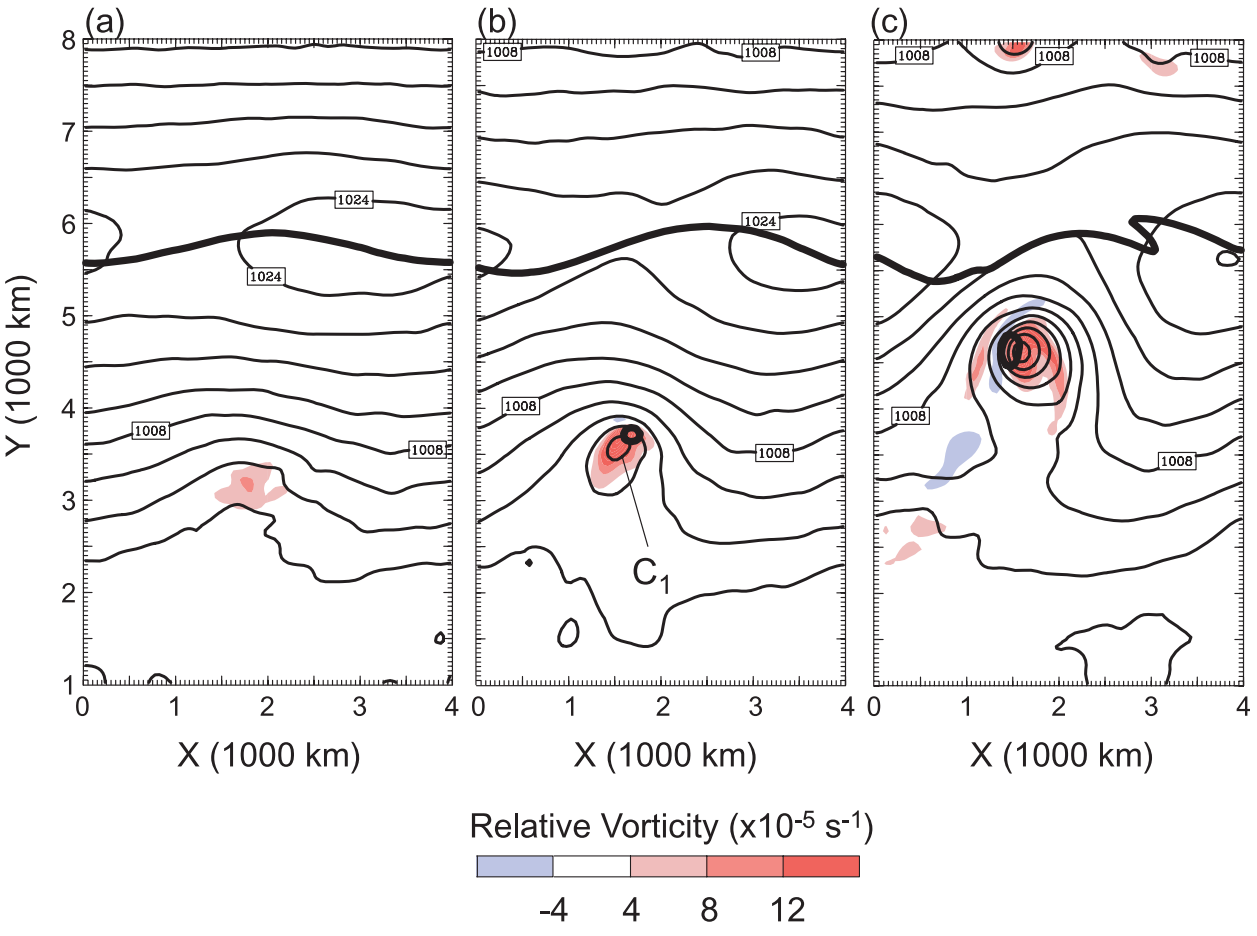

FIG. 3. SLP (CI = 4 hPa), 2-PVU contour (heavy contour) on the 330-K isentropic surface, and relative vorticity at 900 hPa from simulation S15_U30 at (a) 120, (b) 156, and (c) 192 h.

of the domain near $y = 9000$ km (Figs. 2b,d). Two secondary cyclones have developed in both the dry and moist simulations on the eastern and southeastern flank of the cyclonic PV feature. These are located along $y = 7500$ km and $y = 5000$ km. In the moist simulation a separate cyclone (C_3) has developed still farther south near $y = 3000$ km. This cyclone has a region of heavy rainfall on its northern flank. Boundary layer temperature (not shown) indicates that a warm frontal structure coexists with the heavy rainfall and a weak cold front extends south of the cyclone with attendant light convective precipitation.

A graphical summary of the simulations shown in Fig. 2 is obtained by constructing a Hovmöller diagram of the maximum PV at each latitude on the 330-K surface, $q_{\max}(y, t)$. In addition, it is useful to compute the fraction of PV along a given latitude above or below a fixed value. Condensation heating is expected to change such a fraction irreversibly. We compute the fraction of PV less than 1 PVU as a function of y, termed $q_{\text{frac}}(y, t)$. Hence a value of 0.75 means that PV was less than 1 PVU over 75% of the zonal extent of the domain at that latitude.

The Hovmöller diagrams of $q_{\text{frac}}(y, t)$ and $q_{\max}(y, t)$ support the statement that condensation heating qualitatively changes the solution in S15_U30 (Figs. 4a,b). Initially both quantities have a simple meridional variation, with $q_{\text{frac}}(y, t)$ essentially constant north and south of a narrow transition zone and $q_{\max}(y, t)$ representing the initial variation of PV on the 330-K surface (see Fig. 1a). The result of condensation heating in S15_U30 is clearly a dramatic increase in the meridional rearrangement of PV relative to what happens in the dry simulation. Not only is there enhanced anticyclone development at high latitudes, but high PV is transported to low latitudes where it then influences further cyclone development.

The tracks of cyclones moving poleward from lower latitudes are seen as ribbons of enhanced maximum PV values in the simulations with condensation heating. In

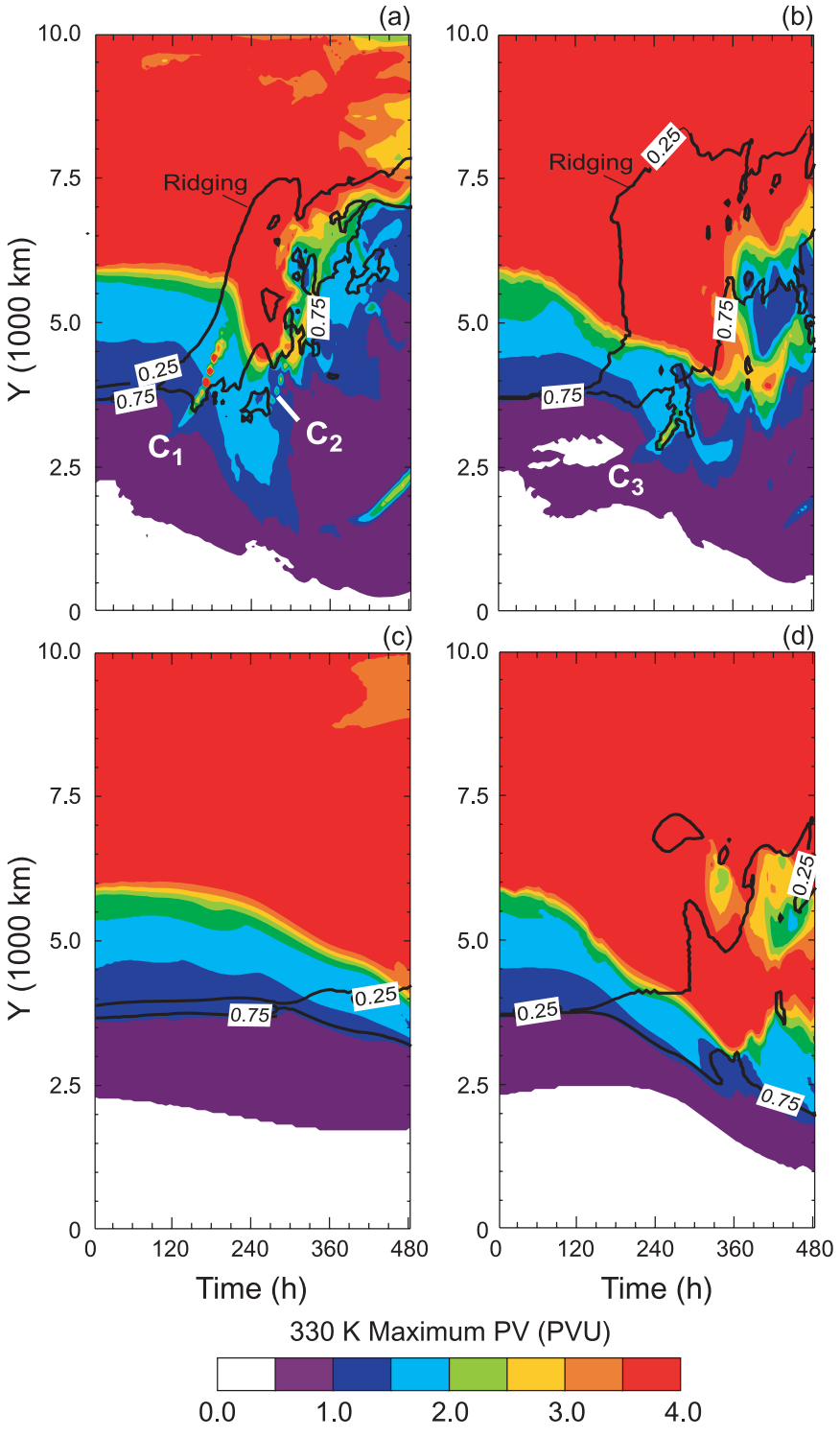

FIG. 4. Hovmöller diagrams of q_{max} (color, PVU) and q_{frac} (0.25 and 0.75 contours) as a function of y and t for (a) S15_U30, (b) S15_U40, (c) S15_U30_D, and (d) S15_U40_D.

S15_U30 (Fig. 4a), the effect of the cyclone is to rapidly build a ridge through diabatic processes. This is seen primarily in the $q_{\text{frac}}(y, t)$ parameter. Ridge development in S15_U30 follows the poleward movement of cyclone C_1 (Fig. 4a) while another cyclone, C_2, forms at relatively low latitudes and migrates poleward. No low-latitude cyclones form in the dry simulation.

As seen in Fig. 2, the differences between dry and moist simulations with a stronger jet (Figs. 4b,d) are not as pronounced as with the weaker jet (Figs. 4a,c), although the condensation effects are distinctly evident in the rapid appearance of lower PV values at high latitudes around 180 h. In S15_U40, the rapid ridge development occurs *prior* to the formation of cyclone C_3 (Fig. 4b) at low latitudes. This ridge development is part of the development of the primary extratropical baroclinic wave. The low-latitude cyclone dissipates before moving into the midlatitudes, in contrast to the low-latitude cyclone developments in S15_U30.

4. Subtropical cyclones

In this section, we examine the dynamics of the low-latitude cyclones that form in the moist simulations. The primary tools are the set of cyclone-following diagnostics outlined in section 2. Our definition of a subtropical cyclone will be one in which the initial development features negligible baroclinicity and significant lower-to-middle-tropospheric PV (assumed to originate from diabatic heating) such that the ratio PV1/PV2 is nearly zero. Furthermore, to distinguish subtropical and tropical cyclones, we insist on deep and relatively strong vertical wind shear oriented generally from a westerly direction during the development process. Here ''strong'' means at least 10–15 m s^{-1} of shear over the troposphere between 900 and 300 hPa. DeMaria et al. (2001) noted that tropical cyclone formation was exceedingly rare when the zonal component of the wind shear between 850 and 200 hPa was westerly and exceeded 12.5 m s^{-1}.

The first cyclone examined is C_1 from simulation S15_U30. Time series of PV1 and PV2 parameters indicate that this cyclone is almost entirely a manifestation of diabatic heating early in its evolution (Fig. 5a). Around the time that the cyclone achieves its maximum intensity the baroclinicity begins increasing notably. But from an equivalent PV perspective, the contribution from baroclinicity always remains far below the interior PV contribution. The vertical wind shear, averaged within a cyclone-centered box 1000 km on a side and expressed as the magnitude of the velocity difference between 900 and 300 hPa, was 16.6 m s^{-1} averaged over the cyclone development stage (90–192 h). The vertical shear at the beginning of the track is westerly at about

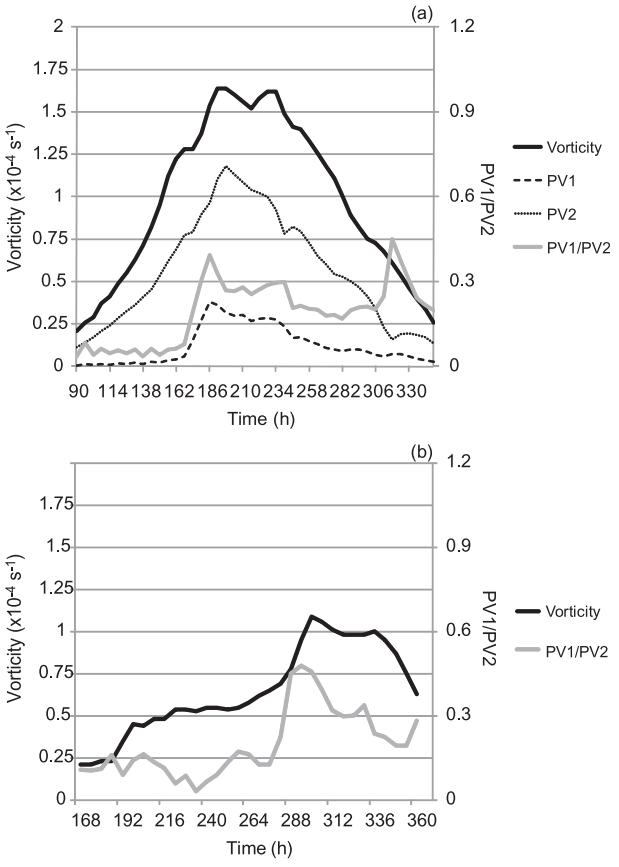

FIG. 5. Time series of (a) vorticity (thin black), PV1 (dashed black), PV2 (thin gray), and PV1/PV2 (thick gray) for cyclone C1 from simulation S15_U30, and (b) vorticity and ratio PV1/PV2 for cyclone C2 from simulation S15_U30. Vorticity is in 10^{-4} s^{-1} and PV is in PVU.

13 m s^{-1}, so it is clear that C_1 experienced moderate vertical wind shear throughout its development. We argue that C_1, because of its dependence on condensation heating, its near absence of lower-tropospheric baroclinicity, and its formation in moderate, deep, westerly shear, should be denoted a subtropical cyclone.

Surface cyclone C_2 forms on the east side of an elongated upper-tropospheric PV filament that forms in response to the outflow from C_1 (Figs. 2a and 4a). The PV time series for this cyclone indicates that it, too, has almost no baroclinic contribution initially and is therefore similar to C_1 (Fig. 5b). The vertical shear over C_2 during its development is southwesterly, averaging around 10 m s^{-1}. Thus, C_2 is also designated as a subtropical cyclone.

The PV parameter time series for the primary cyclone (near $y = 9000$ km in Fig. 2b) in the simulation with the stronger jet ($U = 40$ m s^{-1}) is consistent with expectations of PV components of a growing baroclinic wave. The time series of the primary cyclone in the fake-dry simulation (S15_U40_D) is shown in Fig. 6a. This may

be compared with the time series from the moist simulation in Fig. 6b. In both cases the baroclinic contribution dominates the interior PV contribution early on. There appears to be a nontrivial contribution from the interior PV even in the dry simulation. Recall that this simulation was run with a boundary layer parameterization and surface fluxes. We surmise that the positive PV anomaly is produced at the top of the boundary layer as a result of the turbulent mixing below, which redistributes PV in the vertical. The appearance of cyclonic PV anomalies from mixing was described in detail by Stoelinga (1996). In the moist case, the interior PV contribution (PV2) becomes notably larger and the maximum intensity of the cyclone nearly doubles relative to the dry case. We may infer that condensation effects rapidly increase in their importance around the beginning of day 7 (144 h) when the cyclone intensity abruptly increases and departs from the time series for the dry cyclone.

Cyclone C_3 (see Fig. 4b), which later develops in S15_U40, is highlighted in Fig. 6c. The time series shows that the initial cyclone has essentially zero baroclinic contribution, at least as judged by lower-tropospheric temperature gradients. The primarily influence is the cyclonic PV in the lower troposphere that we infer arises from condensation heating. Near the time of maximum intensity of this cyclone, baroclinic influences become more prominent. Although the details differ, this cyclone is similar in its PV partitions to cyclones C_1 and C_2 from S15_U30. Note also that the vertical shear between 900 and 300 hPa averaged about 14 m s^{-1} from a westerly direction during the development phase, again similar to C_1. Given its similarity with C_1 and C_2, we term C_3 a subtropical cyclone as well.

Cyclone C_3 emerges following the development of a Rossby wave on the tropopause in conjunction with the formation of a subtropical jet stream, but also apparently with some influence from the southward penetration of the primary trough from the midlatitude baroclinic wave. Recall that in simulation S15_U30 the subtropical cyclone developed more rapidly than the extratropical cyclone and hence dominated the solution. In S15_U40, subtropical and extratropical developments overlap in time. Shown in Fig. 7 are maps of potential temperature on the dynamic tropopause θ_{TR}, here defined as a surface of constant PV (=2 PVU). Fields are interpolated vertically to this surface from the two model levels that bracket the PV = 2-PVU surface, based on a downward search starting at the top of the model. The view of Rossby waves from the dynamic tropopause perspective appears in Morgan and Nielsen-Gammon (1998) and is similar to the view of undulating PV contours on an isentropic surface, except here it is represented as undulations of potential temperature contours on a PV surface.

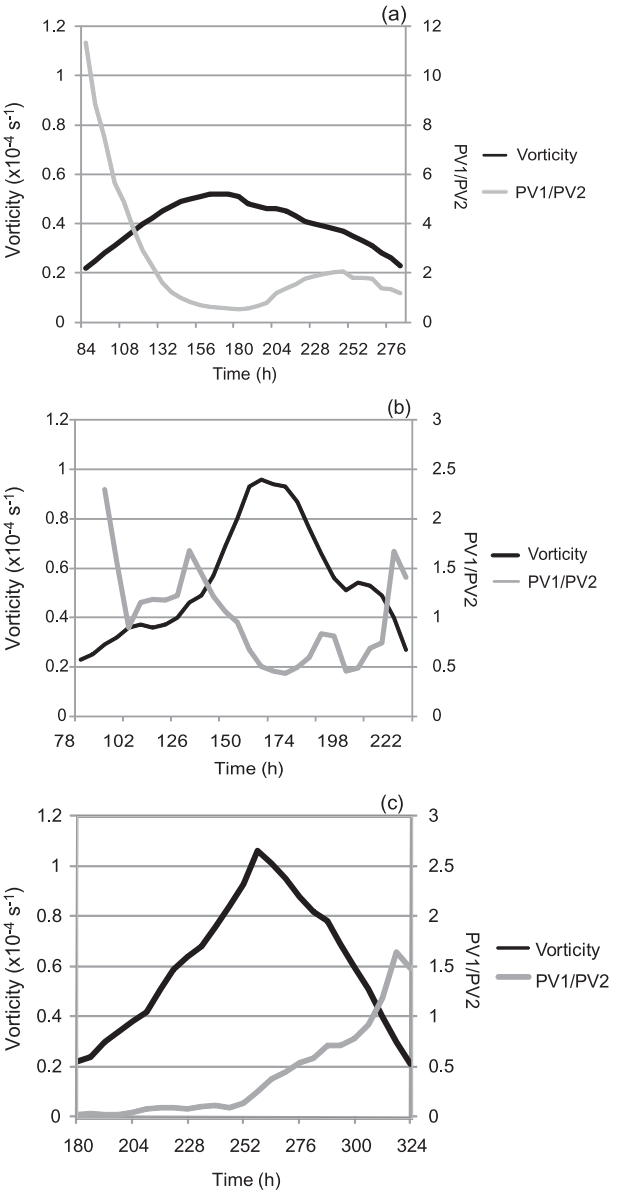

FIG. 6. Time series of maximum area-averaged relative vorticity (black) and ratio PV1/PV2 (gray) for (a) the primary baroclinic cyclone in S15_U40_DRY, (b) the primary baroclinic cyclone in S15_U40, and (c) the secondary (subtropical) cyclone in S15_U40. Vorticity is in 10^{-4} s^{-1}.

At 120 h the undulations of θ_{TR} contours are associated with the primary baroclinic wave development over the northern portion of the domain shown (Fig. 7a; note that the model domain extends 3000 km farther north). Farther south, scattered precipitation, nearly all parameterized, occurs from y = 2000 km to y = 2500 km. A well-defined gradient of potential temperature exists

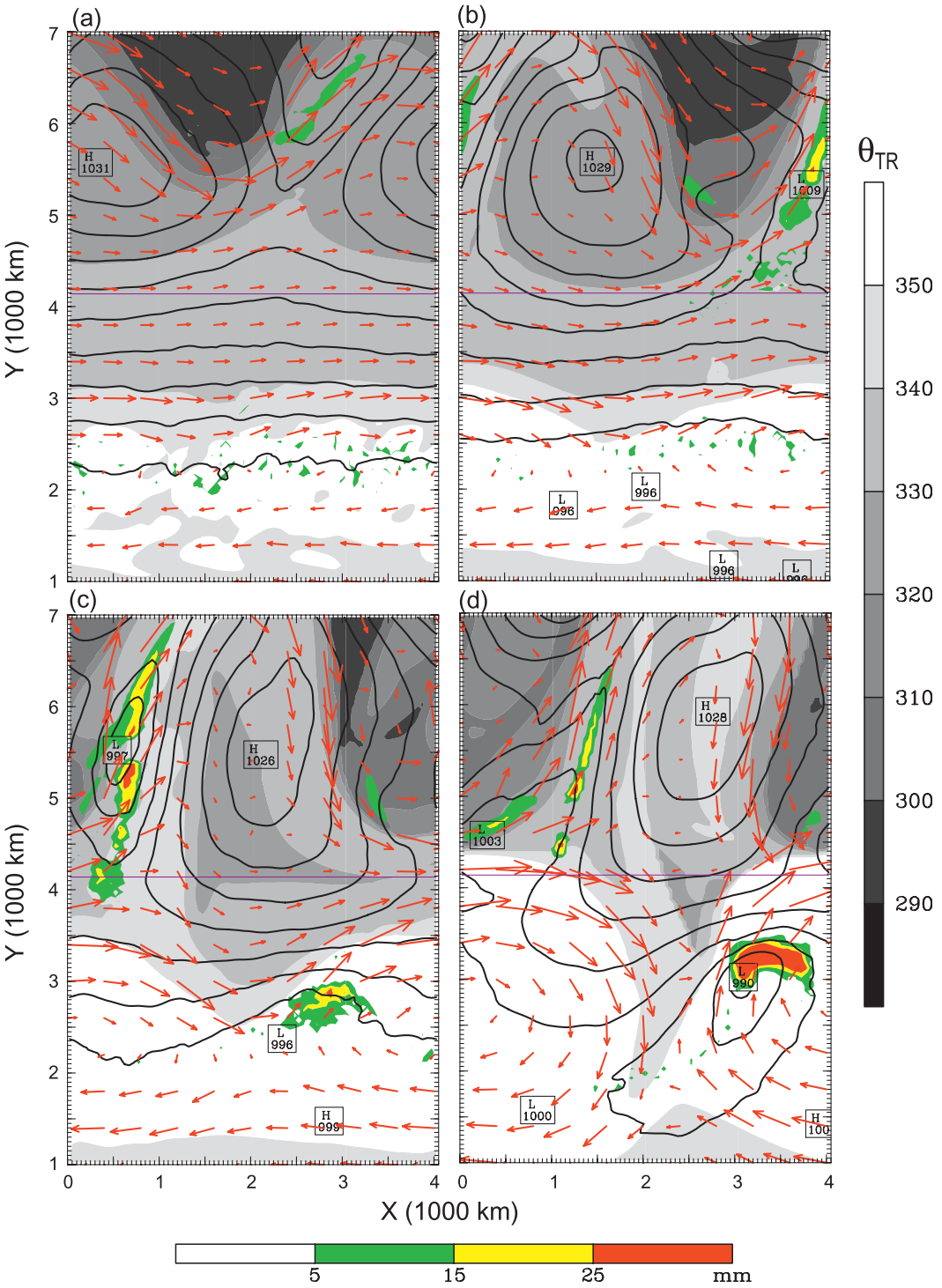

FIG. 7. Maps of θ_{TR} and winds on PV = 2-PVU surface, SLP (CI = 4 hPa) and 6-h accumulated precipitation from simulation S15_U40 at (a) 120, (b) 168, (c) 216, and (d) 264 h. The domain shown spans $y = 1000$ km to $y = 7000$ km. Thin purple zonal line near $y = 4200$ km denotes 26°C SST isotherm.

immediately poleward of this weak convection. By 168 h the low-latitude θ_{TR} contours exhibit waviness, as do the tropopause winds (Fig. 7b). The convection now appears slightly more localized to the east of the trough. This wave amplifies and appears to merge with a southward extrusion of low-θ_{TR} air from the primary baroclinic wave. This forms a relatively robust upper-tropospheric wave by 216 h as a weak cyclone forms at $y = 2500$ km with well-organized deep convection (Fig. 7c). The cyclone then amplifies and intense convection rapidly builds an anticyclone on the tropopause with attendant strong westerlies on the poleward flank of the tropopause anticyclone near $y = 4500$ km (Fig. 7d).

On the equatorward side of the tropopause anticyclone there is an easterly jet, but there is little hint of undulation of the associated potential temperature gradient until the subtropical cyclone is well developed (Figs. 7c,d). The lack of development on the easterly jet is probably due to the near absence of surface winds that might destabilize the atmosphere with respect to moist convection.

Viewed from an eddy and mean-flow perspective on the tropopause, it is clear that the early convection in the moist simulation fundamentally changes the zonal mean of θ on the tropopause by forming a local maximum over the southern part of the domain (Figs. 8a,c). To assist with interpretation we have integrated a separate simulation beginning with the moist-simulation state at 120 h but thereafter allowing no condensation heating or cooling (simulation S15_U40_D120). This simulation maintains a sharpened gradient of θ_{TR} near $y = 2500$ km as well as the minimum of θ_{TR} further south. This sharpened gradient of θ_{TR} corresponds to a secondary zonal wind maximum that we interpret as a subtropical jet. In S15_U40_D120 this jet remains anchored at $y = 2500$ km, but in the moist simulation the jet moves poleward with time as the subtropical storm amplifies (Fig. 8a).

Furthermore, it appears that the midlatitude wave influences the subtropical disturbance beginning around day 8 based on the eddy fluxes of θ_{TR} (Fig. 8b). Here the analogy of eddy PV flux is the eddy flux of potential temperature on the tropopause. Positive fluxes indicate wave amplification and changes in the zonal mean. To assess the influence of the extratropical baroclinic wave on the low-latitude cyclone formation, we integrated an additional simulation (S15_U40_NOMODE) in which the initial normal mode amplitude was set to 0.001 K. Development of a subtropical cyclone proceeded somewhat like that shown in Fig. 7 but with no discernable influence from midlatitudes (Fig. 8h). In fact, the resulting cyclone became a powerful cyclone in the extratropics, similar to the evolution of the subtropical cyclone in S15_U30 (Fig. 2a). More description of simulation S15_U40_NOMODE can be found at the end of section 5.

In each simulation with condensation heating during the first five days, the redistribution of PV due to the heating produces a zonally averaged state with a reversal of the meridional PV gradient on isentropic surfaces, and a reversal of the meridional gradient of potential temperature on the tropopause. The former can clearly be seen in Fig. 9b. In comparison, Fig. 9a shows no reversal of the PV gradient. Because of this reversal of PV or θ_{TR} gradients, we infer that the necessary condition for baroclinic or mixed barotropic and baroclinic instability is satisfied. If the heating is shut off after day 5, there eventually emerges a growing mode structure on the subtropical jet around day 10 (Fig. 8d), but wave growth is slow in comparison with growth on the midlatitude jet without diabatic heating (e.g., Fig. 8f).

Two points may be inferred from the preceding analysis. First, the midlatitude baroclinic wave in S15_U40 is mainly a hindrance to the full development of the subtropical cyclone. We surmise that the negative influence is both through increasing horizontal deformation and vertical wind shear associated with the southward-moving polar front. However, because the initial development of the subtropical cyclone does not depend appreciably on the midlatitude baroclinic wave, the phase relation between the two systems is effectively random. This means that the inhibiting configuration of the midlatitude system in the present simulation may depend on the detailed phase relation of midlatitude and subtropical systems. Such is the case in extratropical transition (Ritchie and Elsberry 2007).

The second point is that the development of the subtropical cyclone results from a moist instability of the subtropical jet. There is no evidence of such a disturbance, of any amplitude, in the adiabatic simulation. Even in a basic state with a subtropical jet and reversal of the PV gradient, the disturbance grows slowly without condensation heating. Once heating is allowed the disturbance grows rapidly. This sharply contrasts with the midlatitude development wherein the inclusion of diabatic heating provides a modest enhancement of growth. Part of this difference may be anticipated because of the enhanced water vapor mixing ratio available to the subtropical disturbance owing to its development over warm water. This issue will be addressed in section 5.

A remaining question is how wave activity on the tropopause affects the tropospheric thermodynamic state to promote deep convection. To address this we solve the quasigeostrophic omega equation as described in section 2, using the model-derived geopotential field from S15_U40_D120 at 168 and 216 h (Fig. 10). Vertical cross sections show that the lifting is weak but persistent and

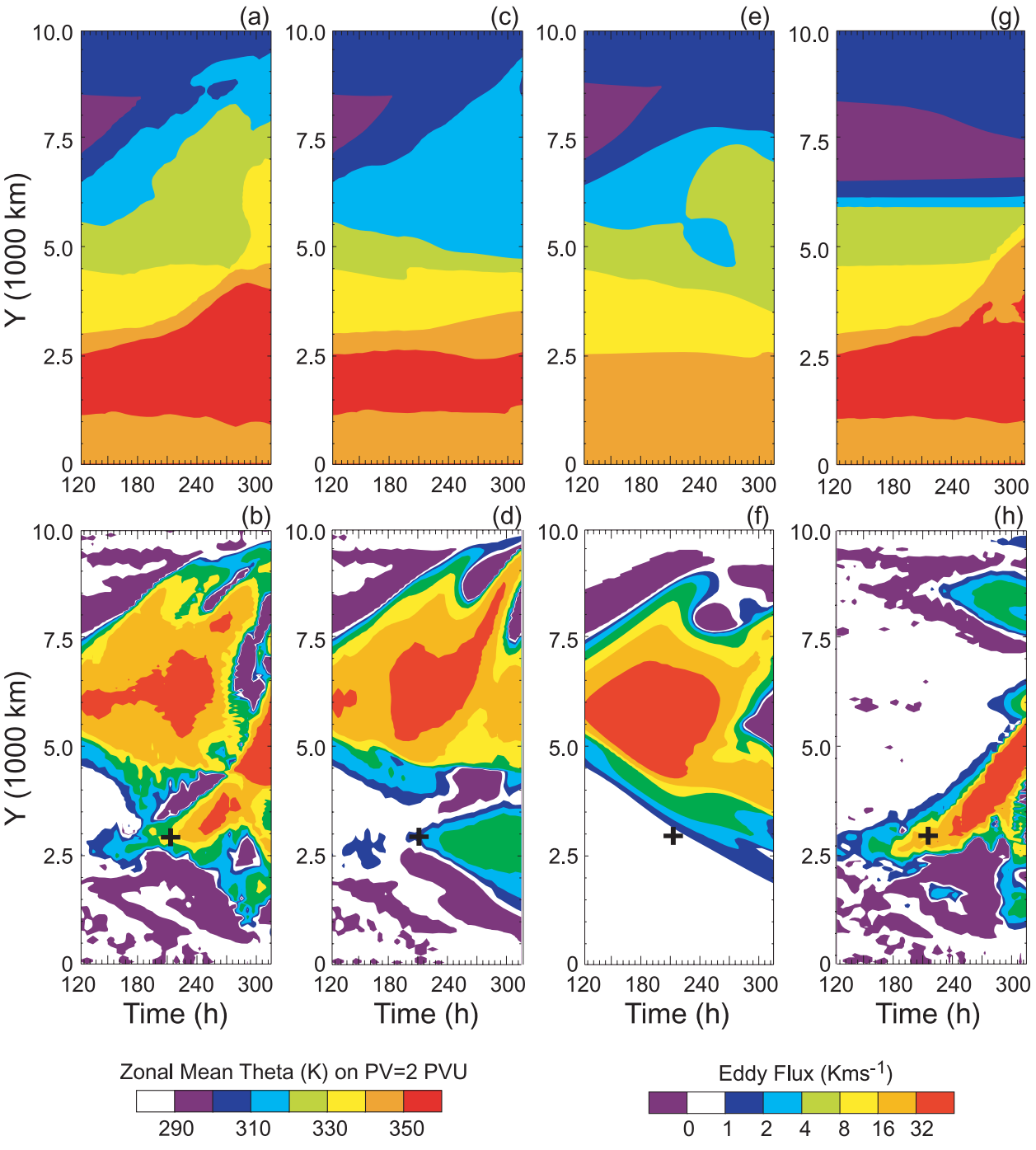

FIG. 8. Hovmöller (y vs t) of (left) zonal mean θ_{TR} and (right) eddy flux of θ_{TR} on the dynamic tropopause, for (a),(b) simulation S15_U40, (c),(d) S15_U40_D120, (e),(f) S15_U40_D, and (g),(h) S15_U40_NOMODE. The cross in the bottom panels is a reference marker that marks the beginning of wave growth on the subtropical jet in S15_U40_D120.

located on the downshear (east) side of the tropopause-based trough. The relative humidity responds by increasing to nearly 80% over a deep layer. Lifting of 0.5 cm s^{-1} produces a vertical displacement of about 1 km in 2 days, which can easily increase the humidity by 20%–30%. In Fig. 10 we also note that there is essentially no meridional velocity signature of the wave in the middle and lower troposphere. Rather, the structure resembles an evanescent wave on the tropopause. In this circumstance, the lifting is almost entirely due to the tropopause

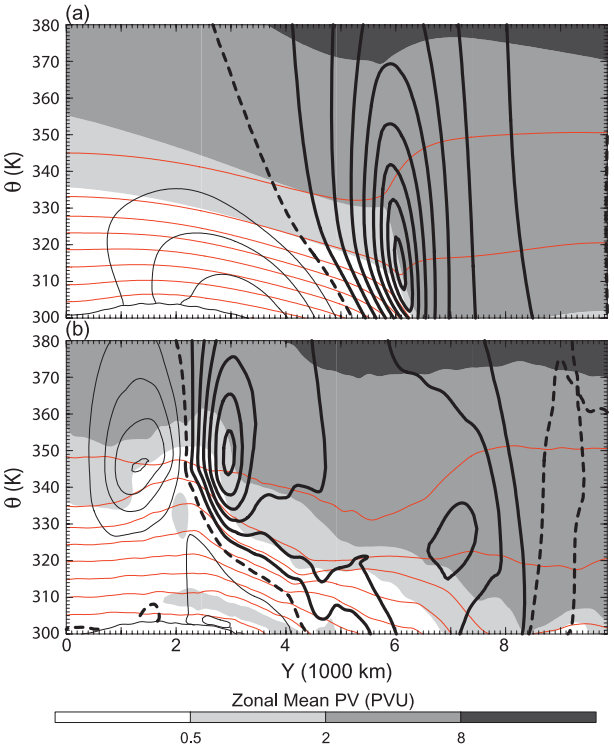

FIG. 9. Zonally averaged cross sections of zonal wind (black; CI = 5 m s^{-1}), PV (grayscale; PVU) and pressure (red; CI = 100 hPa). The vertical coordinate is θ. Times shown are (a) $t = 0$ h and (b) $t = 180$ h from simulation S15_U40. The zero wind line is dashed. Flow into the page is shown with thin solid lines.

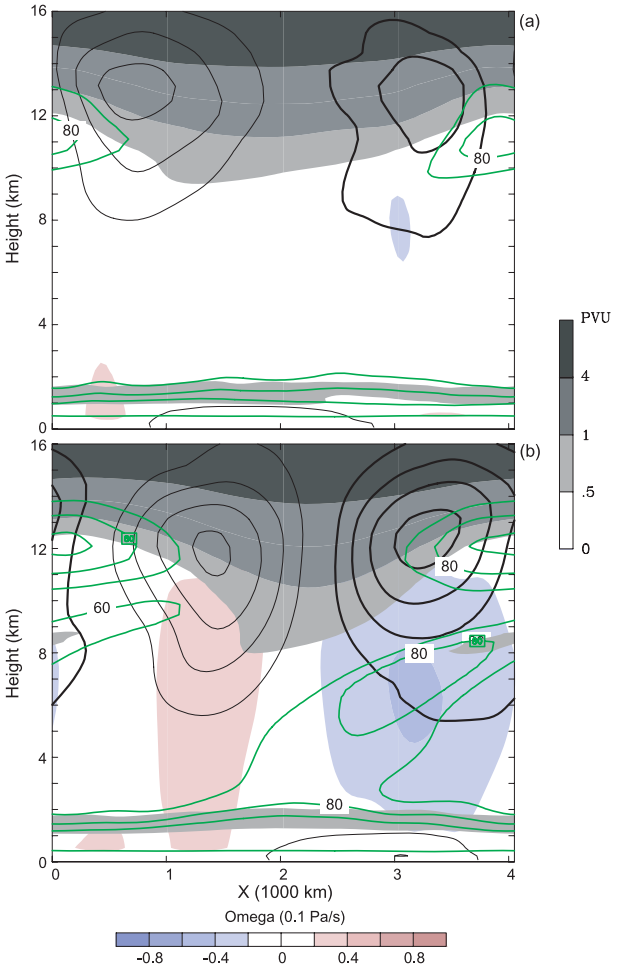

FIG. 10. Quasigeostrophic ω [0.1 Pa s^{-1} (i.e., μb s^{-1}); blue denotes upward motion], PV (grayscale; PVU), meridional wind (zero line omitted; heavy lines for positive values; CI = 2 m s^{-1}), and relative humidity (CI = 20%, beginning at 60%). Cross sections are oriented west–east, centered at $y = 3000$ km and averaged 250 km north and south of the centerline. Fields are shown at (a) 168 and (b) 216 h, both from simulation S15_U40_D120.

perturbation. Juckes and Smith (2000) investigated the convective destabilization from lifting induced by tropopause-based troughs in tropical atmospheres and concluded that even modest tropopause-based troughs can dramatically reduce CIN and increase CAPE. The present results appear consistent with that idea.

In the moist simulation, however, once convection organizes there is generation of surface cyclonic vorticity and eventually a deep cyclone results (Fig. 11). There is a signature of a PV anomaly produced by condensation in the middle troposphere. Note that the adiabatic quasigeostrophic omega is also much larger during cyclogenesis. The structure depicted in Fig. 11 appears similar to that of a baroclinic cyclone, but there is almost zero baroclinicity in the lower troposphere during the early stages of development. Baroclinicity eventually increases as the cyclone develops, especially after the cyclone moves to higher latitudes.

5. Other simulations

In this section we examine the overall sensitivity of results to varying the basic-state vertical and horizontal shear as well as sensitivity to use of different parameterizations. In Fig. 12 are shown results from experiments with varying bottom shear and westerly jet strength at either 240 or 264 h depending on the simulation. Across the top row, the bottom shear is a constant $S = 15$ m s^{-1} whereas the jet strength U is 25, 35, and 50 m s^{-1} in panels a, b, and c, respectively. Much like the first simulation shown in Fig. 1, S15_U25 produces a strong cyclone at low latitudes that becomes a powerful extratropical cyclone (Fig. 12a). This is perhaps not surprising because we already argued that baroclinic waves on a westerly jet of 30 m s^{-1} did not grow fast enough to influence the low-latitude development. Disturbances on the weaker jet will grow even more slowly. In fact, a simulation in which the midlatitude tropopause jet was

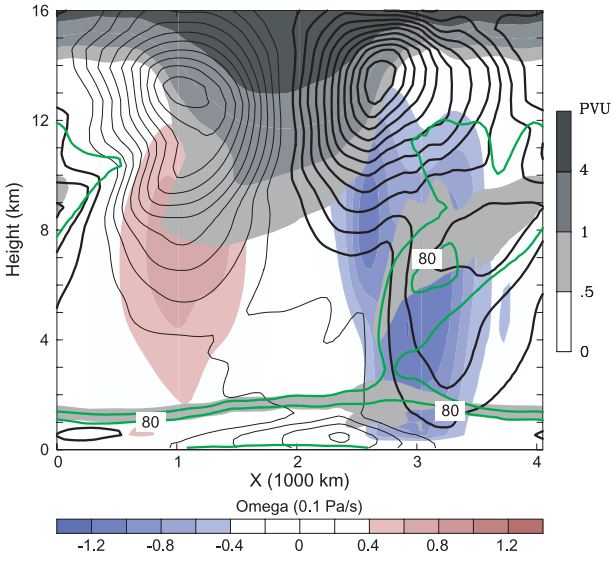

FIG. 11. As in Fig. 10, but for simulation S15_U40 at 216 h.

completely removed produced a subtropical cyclone development qualitatively similar to that shown in Fig. 12a (not shown). The cyclone shown in Fig. 12a is a subtropical cyclone by our definition.

In S15_U35 (Fig. 12b), the result parallels S15_U40 in that a low-latitude cyclone emerges with a similar structure. Simulation S15_U35 also presents a competition between the subtropical cyclone development and the southward development of the cyclonic PV trough from midlatitudes. Outflow from subtropical convection intensifies the westerlies near the central latitude of the domain. This westerly subtropical jet appears to impede the southward progression of the extratropical trough by literally stripping PV from the trough through strong horizontal shear. The associated ''barrier'' effect (Dritschel and McIntyre 2008, and references therein) is well known to occur on the edge of the polar jet. However, careful comparison of Fig. 12b and Fig. 7d reveals that the zonal phase relationship between the subtropical cyclone and baroclinic wave is different from that in S15_U40. While the subtropical cyclone in S15_U40 decays after 264 h, the subtropical cyclone in S15_U35 becomes positioned to the east of the midlatitude trough and enjoys a period of renewed development at higher latitudes (not shown).

In the simulation with the strongest jet, S15_U50 (Fig. 12c), no subtropical cyclone develops. A frontal secondary cyclone forms primarily through baroclinic processes. The influence of the primary baroclinic wave, manifested as a southward extrusion of high-PV air, is strongest in S15_U50. Note that the basic state for this simulation, and the resulting evolution, are broadly similar to the LC1 results from Thorncroft et al. (1993).

In the second row of Fig. 12 are shown results from two simulations where $S = 10$ m s^{-1}. The simulation with $U = 30$ m s^{-1} forms a closed anticyclone on the tropopause wherein the low-PV air that results from the deep convection ''pools'' within the closed circulation (Fig. 12d). A cyclone with subtropical characteristics eventually emerges in this simulation, but not until day 12. When the westerly jet increases to 40 m s^{-1} (Fig. 12e), essentially no subtropical cyclone activity occurs. Secondary cyclone formation occurs in response to the southward-moving trough. Based on the temperature gradients and the gradient of sea level pressure poleward of the cyclone center, the secondary cyclone in S10_U40 is considerably weaker than the one in S15_U50 but the overall behavior is qualitatively similar.

The result from the lone simulation performed with $S = 5$ m s^{-1} is depicted in Fig. 12f, for which $U = 30$ m s^{-1}. This simulation represents a similar evolution to that in S15_U50 and S10_U40, although with the weakest secondary cyclone of all. Thus, it appears that decreasing the westerly jet strength and the bottom shear simultaneously can result in a similar evolution qualitatively.

Time series of PV parameters representing the secondary cyclones in S10_U40 and S05_U30 clearly show that both begin as baroclinic cyclones because PV1/PV2 is near unity or greater (Fig. 13). This distinguishes such cyclones dynamically from subtropical cyclones despite their formation at a relatively low latitude. During the development of these cyclones the vertical wind shear (900–300 hPa) is about 10–15 m s^{-1} from the southwest in S05_U30 and 25–29 m s^{-1} from the south in S10_U40. The latter is nearly twice as large as that found typically for subtropical cyclones in simulations presented earlier. In S05_U30, deep convection does not develop at low latitudes and therefore the subtropical tropopause is largely undisturbed from its initial configuration. With the weak surface winds that accompany $S = 5$ m s^{-1}, the thermodynamic destabilization from moisture fluxes from the ocean is relatively absent and deep convection does not develop. As a consequence, there is little diabatically induced PV change in the upper troposphere and the subtropical jet stream remains weak.

All the simulations discussed so far used essentially the same thermodynamic profile over the southern part of the domain, namely, with relatively large CAPE of roughly 3000 J kg^{-1} for the most unstable, undilute parcel. The large CAPE was partly a response to fluxes of water vapor from the ocean. These fluxes also destabilized the atmosphere by reducing CIN. It is clear that deep convection was responsible for altering the basic state to produce a subtropical jet on the dynamic tropopause. A reasonable question is therefore how sensitive this behavior is to the thermodynamic state. In

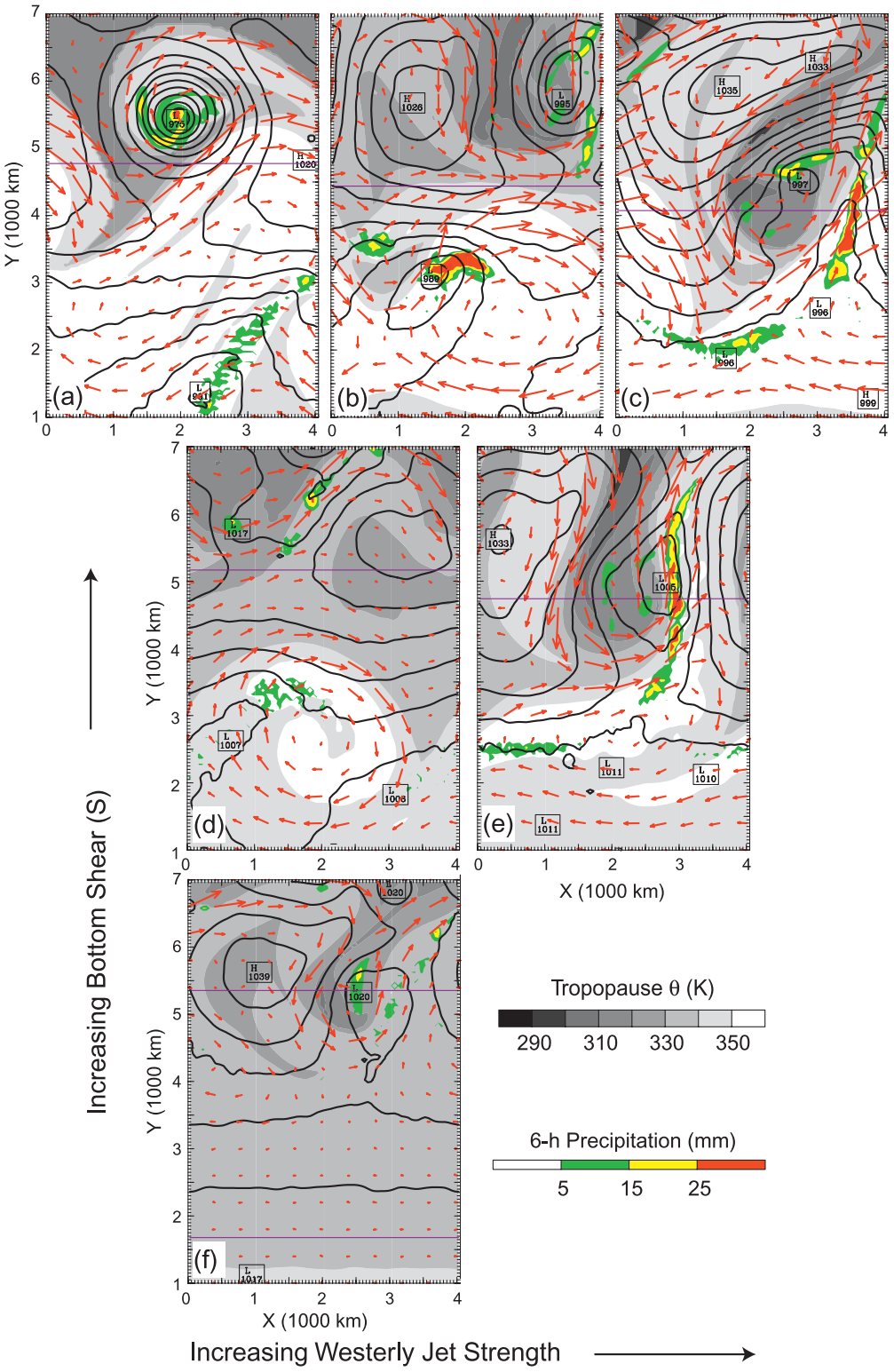

FIG. 12. Tropopause maps as in Fig. 7, but for (a) S15_U25 at 240 h, (b) S15_U35 at 264 h, (c) S15_U50 at 240 h, (d) S10_U30 at 264 h, (e) S10_U40 at 264 h, and (f) S05_U30 at 264h. The thin purple zonal line denotes the 26°C SST isotherm.

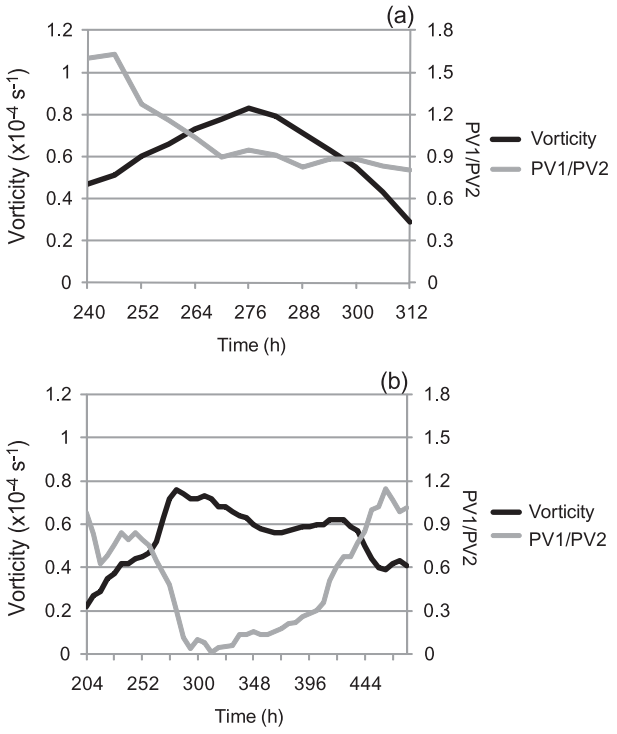

FIG. 13. Time series of cyclone-following maximum vorticity (black) and PV1/PV2 (gray, dimensionless) for secondary cyclones from (a) S10_U40 (cf. Fig. 10e) and (b) S05_U30 (cf. Fig. 10f).

particular, if CAPE were significantly reduced, what would happen?

The most straightforward way to reduce CAPE and the effects of condensation heating in general is to reduce the temperature. This is done by decreasing potential temperature everywhere in the domain by 5 K at the start of the simulation. For a uniform change in potential temperature, the adiabatic normal mode is unaltered. However, this change effectively decreases the tropospheric temperature and SST by the same amount. In this case the maximum SST in the domain is about 25°C, compared to 30°C in all the forecasts discussed previously. This reduction in SST decreases the mixing ratio during the simulation by about 20%. CAPE is reduced by roughly 30% and CIN stays about the same.

The simulations with the reduction in temperature will be denoted by a ''C'' (for ''cooler'') appended to the name. Repeating the two moist simulations shown in Fig. 2 but with lower temperature still results in a subtropical cyclone forming in S15_U30_C, but not in S15_U40_C (Figs. 14a,b). The simulation with the stronger jet produced a robust secondary cyclone beneath the cold trough that was moving equatorward. In another experiment with the same basic state as in S15_U40_C, but with negligible amplitude in the normal mode, a subtropical cyclone formed but required almost 15 days to do so. It is clear that the strength of convection and total condensation heating are important aspects of creating the basic state upon which a subtropical cyclone grows.

Because of the importance of deep moist convection in the formation and intensification of subtropical cyclones in the present model, it is important to examine the sensitivity of results to the cumulus parameterization. Even for a given cumulus scheme, a change in model resolution can produce different results. To investigate the sensitivity to resolution and parameterization choices, we focus on the base state with the 40 m s^{-1} jet. To isolate better the subtropical development from midlatitude development, and therefore enhance the relative importance of diabatic to baroclinic processes, we choose the initial condition with the initial amplitude of 0.001 K. The reference simulation, S15_U40_NOMODE was already discussed in section 4. The other two simulations presented here include one in which the horizontal grid spacing was decreased to 25 km (S15_U40_DX25) and one using the Grell–Dévényi cumulus scheme (Grell and Dévényi 2002) with the standard 50-km grid spacing (S15_U40_GD).

Figure 15 contains a summary of the essential differences between the three simulations. An important difference is the relatively larger values of tropopause potential temperature due to stronger convection in the perturbed simulations between days 3 and 6. This can be seen as a large area of $\theta_{TR} > 360$ K (Figs. 15b,c) in the perturbed simulations, whereas this area hardly exists in the reference simulation and is induced mainly by the developing storm itself (Fig. 15a). The greater convection results in a greater stabilization of the subtropical atmosphere and delays the subsequent development of the subtropical cyclone by several days. Nevertheless, simulation S15_U40_DX25 produces a strong subtropical cyclone (Fig. 15e) similar to that produced in the reference simulation with a similar time scale of intensification once it starts. The slightly poleward location of the storm (Figs. 15b,e) relative to the cyclone in the reference simulation reflects the broadened anticyclone near the tropopause with westerlies displaced poleward.

In S15_U40_GD, the midlatitude baroclinic wave grows faster (Fig. 15c) so that it tends to dominate the development process by days 15–17 (Figs. 15c,f). The faster growth is a result of the greater condensation heating produced by the Grell–Dévényi scheme. Formation of a low-latitude cyclone occurs as in other simulations, but it is not clearly isolated from the higher-latitude cyclone. Despite the apparent influence of the midlatitudes, the cyclone near $y = 3000$ km forms in the near absence of lower-tropospheric baroclinicity and has a PV1/PV2 ratio nearly zero (not shown). Since it

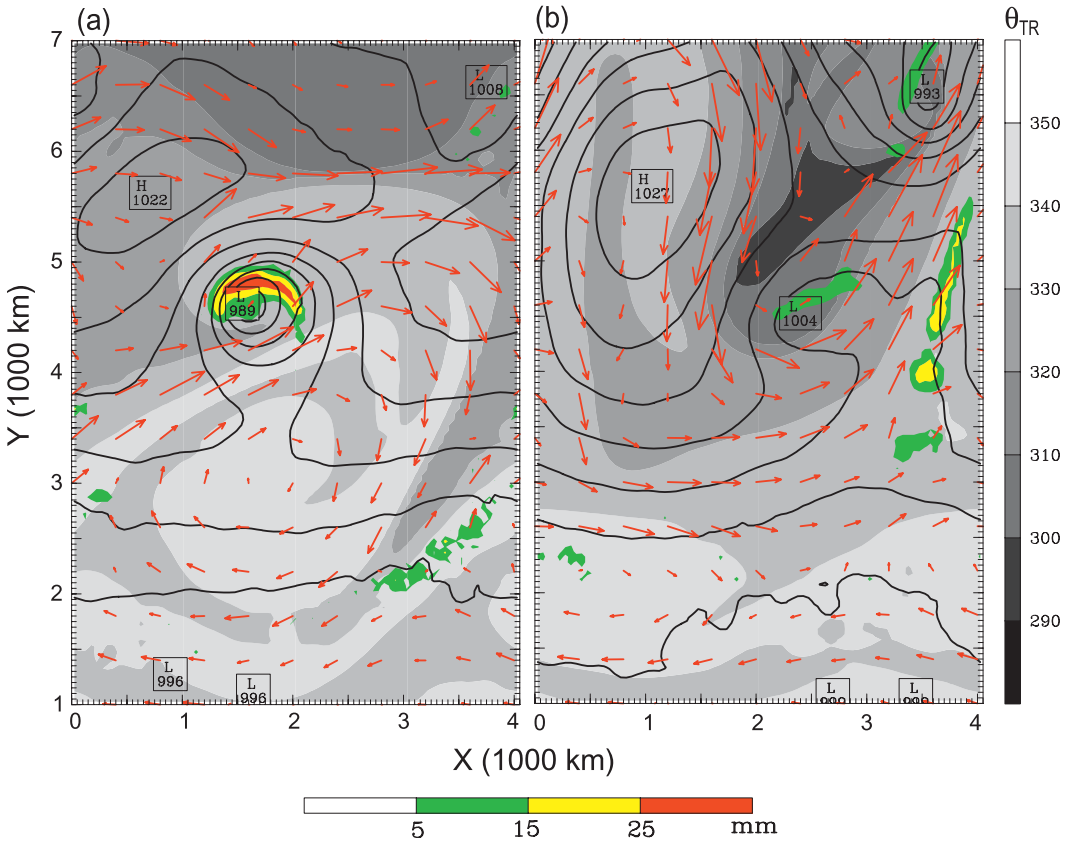

FIG. 14. Tropopause maps as in Fig. 12, but from simulations with initial temperature reduced by 5 K: (a) S15_U30_C, 240 h and (b) S15_U40_C, 264 h.

occurs in westerly shear, this is a subtropical cyclone by our definition. The simulation with the Grell–Dévényi scheme produces more small-scale vortices than the reference simulation, as does the higher-resolution simulation with the Kain–Fritsch scheme, but these vortices appear relatively incidental to the ultimate subtropical development.

6. Conclusions

The present study has utilized idealized, moist primitive equation simulations to define dynamically subtropical cyclones and distinguish these cyclones from extratropical (and tropical) cyclones. The model used was the ARW, initialized with adiabatic normal modes in a baroclinic channel of length 4000 km and width 10 000 km that was entirely over an ocean with prescribed surface temperature. The primary parameters governing the behavior of these simulations appear to be the strength of the westerly jet and the strength of the barotropic shear and surface winds over low latitudes. Barotropic shear and surface winds are linked by the specification of the initial zonal wind on the lower boundary. The former causes anticyclonic wave breaking of the midlatitude Rossby waves. The latter cause convective destabilization through surface fluxes where surface easterlies coincide with the highest sea surface temperatures.

The important parameters are S, the amplitude of the sinusoidally varying "bottom shear," and U, the initial maximum zonal westerly wind. When the ratio $U/2S$ is significantly greater than unity, simulations are dominated by the evolution of the midlatitude baroclinic wave. A variety of cyclones forms within this wave. The primary cyclone is part of the normal mode that initializes the simulation. As the wave becomes nonlinear, additional surface cyclones form on the flank of the large-amplitude cyclonic tropopause PV anomaly. These cyclones tend to form successively farther south as the cyclonic PV trough penetrates to lower latitudes. The southward penetration increases for increasing U. This scenario is represented by the schema in the left column of Fig. 16.

For $U/2S \sim 1$, both midlatitude and low-latitude cyclones form. The formation of the low-latitude cyclone appears to be roughly independent of the midlatitude cyclone. It results from an alteration of the basic state by

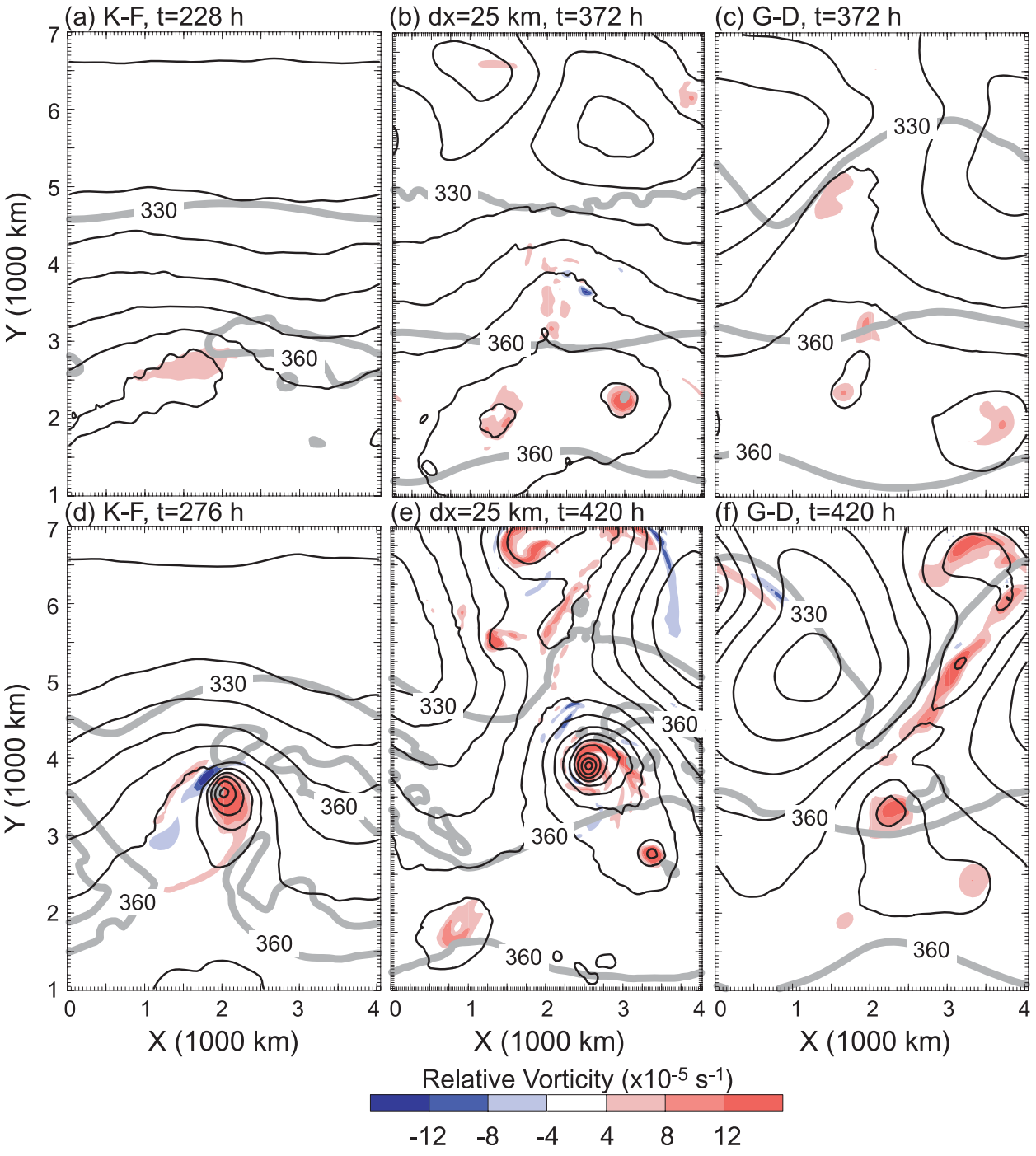

FIG. 15. SLP (CI = 4 hPa), relative vorticity at 900 hPa (color shaded), and θ_{TR} (thick gray lines) for simulations initialized with a 40 m s^{-1} jet with normal mode amplitude set to 0.001 K; (a),(d) Kain–Fritsch cumulus scheme (same as previously discussed simulations at 228 and 276 h, respectively); (b),(e) grid spacing of 25 km, still with the Kain–Fritsch scheme, at 372 and 420 h, respectively; and (c),(f) Grell–Dévényi scheme with a grid spacing of 50 km at 372 and 420 h, respectively.

convection that, in turn, results from thermodynamic destabilization of the troposphere to moist convection where surface moisture fluxes are strongest. The basic state modified by convection supports moist baroclinic instability that manifests itself as a subtropical cyclone growing with a minimum of surface baroclinicity in the presence of deep westerly vertical wind shear. This evolution, summarized in the schema in the right column

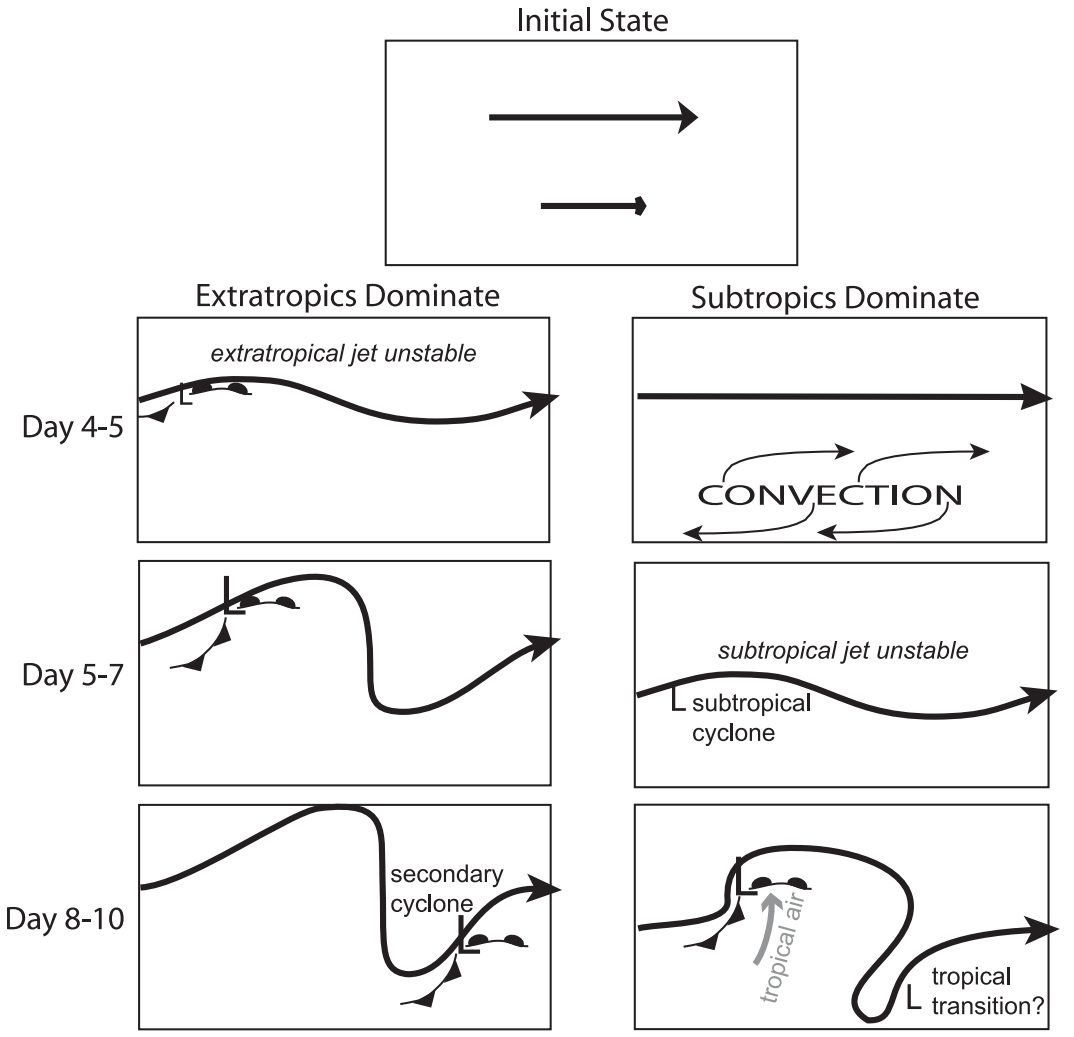

FIG. 16. Schema representing two idealized development pathways. Each panel depicts the axis of either the extratropical or subtropical jet stream (heavy solid line with arrow), the position of major surface cyclones (L's), and cold and warm fronts. Large L's indicate mature cyclones; small L's indicate incipient cyclones.

of Fig. 16, resembles qualitatively that discussed by Montgomery and Farrell (1993), but here the basic state and the perturbations evolve rather than being prescribed.

Whether the subtropical cyclone becomes a dominant midlatitude system depends on the relative rates of growth of the midlatitude and subtropical systems and their spatial phase relation with each other. While it appears that there is often competition between subtropical and midlatitude systems, there are instances in which the subtropical cyclone moves into midlatitudes as a strong cyclone. This situation is similar to the variety of cyclone outcomes possible in extratropical transition.

We devised a metric that describes the relative PV contributions from near-surface baroclinicity (PV1) and cyclonic PV in the lower and middle troposphere (PV2). For $U/2S \gg 1$, all cyclones originate with PV1 $\gtrsim$ PV2 and are therefore primarily of baroclinic origin. For $U/2S \sim 1$, cyclones originate at low latitudes and are characterized by PV1/PV2 $\ll 1$ initially. They form in the presence of moderate westerly shear and synoptic-scale disturbances of modest amplitude. These waves initiate as Rossby waves on the subtropical dynamic tropopause. They destabilize the troposphere and organize deep, moist convection from which the surface cyclone grows. We identify this class of cyclones as subtropical cyclones in a dynamical, rather than geographical, sense. They are distinguished from secondary cyclones such as frontal cyclones (Thorncroft and Hoskins 1990) and real-world cyclones such as kona lows by the near absence of surface baroclinicity. Yet, the formation of subtropical cyclones fundamentally requires deep vertical wind shear and quasigeostrophic dynamics. In this way, subtropical

cyclones are also distinct from the majority of tropical cyclones forming in the deep tropics. In their mature stage, subtropical cyclones may evolve into either baroclinic or tropical cyclones.

Subtropical cyclones, by our definition, belong to a general class of previously identified cyclonic disturbances in which the principal agent of development is condensation heating, but where there is a guiding, baroclinic structure that organizes the heating. Such related disturbances include mesoscale convective vortices initiated and modulated by weak baroclinic waves, diabatic Rossby vortices, and possibly many instances of high-latitude cyclones over warm water such as polar lows and Mediterranean cyclones. It is possible that all such cyclonic systems are manifestations of a similar set of dynamics.

The present paper has not addressed the formation of tropical cyclones from subtropical cyclones. Part of this is because we do not have the model resolution to properly form the inner core structure that characterizes a tropical cyclone. However, it is worth noting that many previous studies have shown that tropical cyclones do form from subtropical cyclones and occasionally from secondary cyclones, with the terms ''subtropical'' and ''secondary'' following the above definitions. The final schematic of Fig. 16 suggests the possibility of a ''tropical transition'' (Davis and Bosart 2004) occurring on the east side of the cyclonic filament of PV at low latitudes.

While the basic knowledge of the nature of subtropical cyclones and their behavior gleaned from our simulations appears internally consistent and consistent with the modest amount of literature on the topic, some words of caution are probably worthwhile. First, we have barely begun to explore the parameter space of this moist baroclinic dynamics problem. It would be useful to perform experiments that attempt to separate the destabilization effects from moisture fluxes induced by the imposed surface winds from the effects of barotropic shear. Furthermore, the transition of secondary and subtropical cyclones to tropical cyclones needs to be thoroughly investigated in order to provide the topic of tropical transition with a more theoretical context.

Acknowledgments. The author is indebted to Riwal Plougenvan of LMD Paris for providing the code and scripts that modified the WRF baroclinic wave test case for more general applications. The paper also benefitted from discussions with Rich Rotunno of NCAR.

REFERENCES

Bluestein, H. B., 1992: *Synoptic–Dynamic Meteorology in Midlatitudes*. Vol. I, *Principles of Kinematics and Dynamics,* Oxford University Press, 431 pp.

Bretherton, F. P., 1966: Baroclinic instability and the short wavelength cut-off in terms of potential vorticity. *Quart. J. Roy. Meteor. Soc.,* **92,** 335–345.

Conzemius, R. J., R. W. Moore, M. T. Montgomery, and C. A. Davis, 2007: Mesoscale convective vortex formation in a weakly sheared moist neutral environment. *J. Atmos. Sci.,* **64,** 1443–1466.

Daingerfield, L. H., 1921: Kona storms. *Mon. Wea. Rev.,* **49,** 327–329.

Davies, H. C., Ch. Schär and H. Wernli, 1991: The palette of fronts and cyclones within a baroclinic wave development. *J. Atmos. Sci.,* **48,** 1666–1689.

Davis, C. A., and L. F. Bosart, 2003: Baroclinically induced tropical cyclogenesis. *Mon. Wea. Rev.,* **131,** 2730–2747.

——, and ——, 2004: The TT problem: Forecasting the tropical transition of cyclones. *Bull. Amer. Meteor. Soc.,* **85,** 1657–1662.

——, C. Snyder, and A. Didlake, 2008: A vortex-based perspective of eastern Pacific tropical cyclone formation. *Mon. Wea. Rev.,* **136,** 2461–2477.

DeMaria, M., J. A. Knaff, and B. H. Connell, 2001: A tropical cyclone genesis parameter for the tropical Atlantic. *Wea. Forecasting,* **16,** 219–233.

Dritschel, D. A., and M. E. McIntyre, 2008: Multiple jets as PV staircases: The Phillips effect and the resilience of eddy-transport barriers. *J. Atmos. Sci.,* **65,** 855–874.

Emanuel, K. A., M. Fantini, and A. J. Thorpe, 1987: Baroclinic instability in an environment of small stability to slantwise moist convection. Part I: Two-dimensional models. *J. Atmos. Sci.,* **44,** 1559–1573.

Evans, J. L., and M. P. Guishard, 2009: Atlantic subtropical storms. Part I: Diagnostic criteria and composite analysis. *Mon. Wea. Rev.,* **137,** 2065–2080.

Grell, G. A., and D. Dévényi, 2002: A generalized approach to parameterizing convection combining ensemble and data assimilation techniques. *Geophys. Res. Lett.,* **29,** 1693, doi:10.1029/2002GL015311.

Guishard, M. P., J. L. Evans, and R. E. Hart, 2009: Atlantic subtropical storms. Part II: Climatology. *J. Climate,* **22,** 3574–3594.

Hart, R. E., 2003: A cyclone phase space derived from thermal wind and thermal asymmetry. *Mon. Wea. Rev.,* **131,** 585–616.

Heckley, W. A., and B. J. Hoskins, 1982: Baroclinic waves and frontogenesis in a non-uniform potential vorticity semi-geostrophic model. *J. Atmos. Sci.,* **39,** 1999–2016.

Juckes, M., and R. K. Smith, 2000: Convective destabilization by upper-level troughs. *Quart. J. Roy. Meteor. Soc.,* **126,** 111–123.

Kain, J. S., 2004: The Kain–Fritsch convective parameterization: An update. *J. Appl. Meteor.,* **43,** 170–181.

Lorenz, E. N., 1955: Available potential energy and the maintenance of the general circulation. *Tellus,* **7,** 157–167.

Montgomery, M. T., and B. F. Farrell, 1993: Tropical cyclone formation. *J. Atmos. Sci.,* **50,** 285–310.

Moore, R. W., and M. T. Montgomery, 2005: Analysis of an idealized, three-dimensional diabatic Rossby vortex: A coherent structure of the moist baroclinic atmosphere. *J. Atmos. Sci.,* **62,** 2703–2725.

Morgan, M. C., and J. W. Nielsen-Gammon, 1998: Using tropopause maps to diagnose midlatitude weather systems. *Mon. Wea. Rev.,* **126,** 2555–2579.

Noh, Y., W. G. Cheon, S. Y. Hong, and S. Raasch, 2003: Improvement of the K-profile model for the planetary boundary layer based on large eddy simulation data. *Bound.-Layer Meteor.,* **107,** 421–427.

Orlanski, I., 2003: Bifurcation in eddy lifecycles: Implications for storm track variability. *J. Atmos. Sci.,* **60,** 993–1023.

Otkin, J. A., and J. E. Martin, 2004: A synoptic climatology of the subtropical kona storm. *Mon. Wea. Rev.,* **132,** 1502–1517.

Parker, D., and A. J. Thorpe, 1995: Conditional convective heating in a baroclinic atmosphere: A model of convective frontogenesis. *J. Atmos. Sci.,* **52,** 1699–1711.

Plougonven, R., and C. Snyder, 2007: Inertia–gravity waves spontaneously generated by jets and fronts. Part I: Different baroclinic life cycles. *J. Atmos. Sci.,* **64,** 2502–2520.

Raymond, D. J., and H. Jiang, 1990: A theory for long-lived mesoscale convective systems. *J. Atmos. Sci.,* **47,** 3067–3077.

Ritchie, E. A., and R. L. Elsberry, 2007: Simulations of the extratropical transition of tropical cyclones: Phasing between the upper-level trough and tropical cyclones. *Mon. Wea. Rev.,* **135,** 862–876.

Rotunno, R., W. C. Skamarock, and C. Snyder, 1994: An analysis of frontogenesis in numerical simulations of baroclinic waves. *J. Atmos. Sci.,* **51,** 3373–3398.

Shapiro, L. J., and J. L. Franklin, 1995: Potential vorticity in Hurricane Gloria. *Mon. Wea. Rev.,* **123,** 1465–1475.

Simmons, A. J., and B. J. Hoskins, 1978: The life cycles of some nonlinear baroclinic waves. *J. Atmos. Sci.,* **35,** 414–432.

Simpson, R. H., 1952: Evolution of the kona storm, a subtropical cyclone. *J. Meteor.,* **9,** 24–35.

Skamarock, W. C., J. B. Klemp, J. Dudhia, D. O. Gill, D. M. Barker, W. Wang, and J. G. Powers, 2005: A description of the Advanced Research WRF version 2. NCAR Tech. Note TN-468+STR, 88 pp.

Stoelinga, M. T., 1996: A potential vorticity-based study of the role of diabatic heating and friction in a numerically simulated baroclinic cyclone. *Mon. Wea. Rev.,* **124,** 849–874.

Thorncroft, C. D., and B. J. Hoskins, 1990: Frontal cyclogenesis. *J. Atmos. Sci.,* **47,** 2317–2336.

——, ——, and M. E. McIntyre, 1993: Two paradigms of baroclinic-wave life-cycle behavior. *Quart. J. Roy. Meteor. Soc.,* **119,** 17–55.

Wernli, H., R. Fehlmann, and D. Lüthi, 1998: The effect of barotropic shear on upper-level induced cyclogenesis: Semigeostrophic and primitive equation numerical simulations. *J. Atmos. Sci.,* **55,** 2080–2094.

——, S. Dirren, M. Liniger, and M. Zillig, 2002: Dynamical aspects of the life cycle of the winter storm 'Lothar' (24–26 December 1999). *Quart. J. Roy. Meteor. Soc.,* **128,** 405–429.

Whitaker, J. S., and C. A. Davis, 1994: Cyclogenesis in a saturated environment. *J. Atmos. Sci.,* **51,** 889–908.